CHALMERS
UNIVERSITY OF TECHNOLOGY

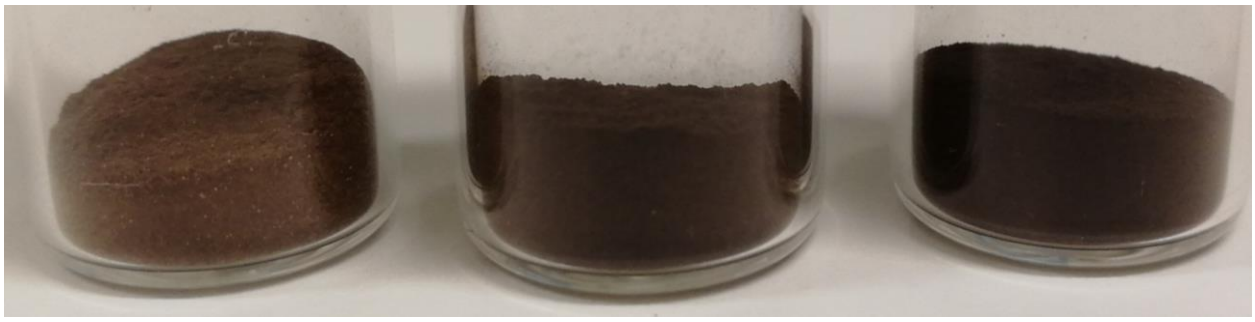

The catalytic properties of Rh/CeO_2 catalysts for the Sabatier reaction

A study of the influence of Rh particle size and the inclusion of Sm- and Fe dopants in the ceria

Master's thesis in Materials Chemistry

Linnea Hammer úr Skúoy

DEPARTMENT OF CHEMISTRY AND CHEMICAL ENGINEERING
CHALMERS UNIVERSITY OF TECHNOLOGY

Gothenburg, Sweden 2022
www.chalmers.se

MASTER'S THESIS 2022

The catalytic properties of Rh/CeO_2 catalysts for the Sabatier reaction

A study of the influence of Rh particle size and the inclusion of Sm- and Fe dopants in the ceria

LINNEA HAMMER ÚR SKÚOY

CHALMERS
UNIVERSITY OF TECHNOLOGY

Department of Chemistry and Chemical Engineering
CHALMERS UNIVERSITY OF TECHNOLOGY
Gothenburg, Sweden 2022

The catalytic properties of Rh/CeO_2 catalysts for the Sabatier reaction
A study of the influence of Rh particle size and the inclusion of Sm- and Fe dopants in the ceria
LINNEA HAMMER ÚR SKÚOY

Supervisor: Per-Anders Carlsson & Felix Hemmingsson, Chalmers University of Technology
Examiner: Per-Anders Carlsson, Chalmers University of Technology

Department of Chemistry and Chemical Engineering
Chalmers University of Technology
SE-412 96 Gothenburg
Sweden
Telephone +46 (0) 31-772 1000

Cover: Photograph of synthesized Rh/CeO_2 catalysts.

Printed by Chalmers University of Technology
Gothenburg, Sweden 2022
The catalytic properties of Rh/CeO_2 catalysts for the Sabatier reaction
A study of the influence of Rh particle size and the inclusion of Sm- and Fe dopants in the ceria
LINNEA HAMMER ÚR SKÚOY
Department of Chemistry and Chemical Engineering
Chalmers University of Technology

Abstract

The demand for fuel increases and efforts are being made to develop renewable alternatives such as biogas and hydrogen gas. However, these have low energy densities but this can be improved by transforming and storing the energy in C-H bonds in other products. One such product is methane, which can be produced through the methanation of carbon dioxide. However, the high stability of carbon dioxide makes a catalyst necessary for the transformation.

In this study, ceria supported rhodium, i.e., 1-3 wt% Rh/CeO_2, where both components have shown promising properties for this reaction, was studied. The aim was to study how Rh particle size affects the catalytic properties, but also to compare obtained results with $Rh/Ce_{1-x}Sm_xO_{2-\delta}$, $Rh/Ce_{1-x}Fe_xO_{2-\delta}$ and $Ce_{1-x}Rh_xO_{2-\delta}$ from another study to see the effects of dopants and the inclusion of Rh in the CeO_2.

The Rh/CeO_2 was synthesized using dry impregnation followed by freeze-drying and calcination. Used characterization methods were XRF, BET and CO chemisorption, with DRIFTS as a complement. The reaction was run using a fixed bed reactor at four different temperatures: 150, 250, 350 and 400 °C.

The results showed a specific surface area in the interval 123-133 m^2/g sample and a decrease in Rh particle size with higher loads of Rh on the ceria. Out of the Rh/CeO_2 samples, the one with the smallest Rh particle size showed the highest reaction rate, while the one with the biggest Rh particle size showed the highest selectivity. It was not possible to directly determine whether the Rh was best used for impregnation or as a dopant due to the reaction rate being higher for Rh/CeO_2 but the selectivity being higher for $Ce_{1-x}Rh_xO_{2-\delta}$. However, $Rh/Ce_{1-x}Sm_xO_{2-\delta}$ turned out to be the most efficient catalyst for this reaction, both in regard of activity as well as selectivity. A Fe dopant generally decreased the catalytic properties.

This study gave an insight to the impact of Rh particle size and the use of dopants, but more experiments need to be done to deem the results statistically significant for more realistic conditions with varying of reaction conditions. Further experiments also need to be done to study more catalytic properties than what was covered in this work.

Acknowledgements

I would like to thank my examiner Per-Anders Carlsson for making this project possible and for answering all my questions.

I would also like to thank my supervisor Felix Hemmingsson for all time put into this project and all help with everything.

Thank you Yuqi for a nice teamwork and to be able to use your results in my project. It has been very fun working with you.

Andreas Schaefer for showing me how the machines work and the theory behind them and for answering all my questions.

The rest of the people at the division for applied chemistry for a good time and for your help.

The people in the office for support and good times/talks.

Finally, I would like to thank my family for all their support and shown interest throughout this project.

Linnea Hammer úr Skúoy, Gothenburg 2022

Contents

List of figures

List of tables

1 Introduction

Higher levels of greenhouse gases in the atmosphere are of great concern. One such gas is the carbon dioxide (CO_2) which, even though it is not by far the most severe greenhouse gas, has gained a lot of attention. [1] Though the CO_2 isn't the worst greenhouse gas in terms of global warming potential, it is produced in great amounts through combustion of fossil fuels as well as being emitted as a byproduct from different industrial processes. However, it is at the same time used by plants in the photosynthesis but the levels are far too high for the plants to compensate which has led to the increased interest of biofuels, fuels made from biomass, where the aim is to have a net CO_2 value of zero.

One downside of the biofuels is the low energy density of biomass compared to e.g. crude oil. The biomass often contains other elements than what is desired and are usually solids with complex structures and a high water content which means that a lot of energy is needed in order to extract the pure biofuels.

The use of hydrogen gas, produced from the water splitting reaction using energy from renewable energy sources, is another option. However, the energy density is low in this product as well but can be increased by using the hydrogen to produce e.g. alcohols and alkanes, where the energy is stored in the C-H bonds. The Sabatier reaction is such a way.

$$\mathrm{CO_2} + 4\mathrm{H_2} \rightleftarrows \mathrm{CH_4} + 2\mathrm{H_2O}$$

One industrial process that could be a possible CO_2 feedstock is the decarbonation of limestone within the cement production, where a significant amount of CO_2 is emitted. [2] If one can capture this CO_2 and turn it to methane (CH_4), which is one of the main components in natural gas, it is possible to create a recirculation of CO_2.

Since CO_2 is a stable molecule there is a need of a catalyst with high activity, as well as high selectivity, for the methane. Nickel (Ni) is commonly used due to its high activity and selectivity as well as low cost. [3, 4] Alumina (Al_2O_3), titania (TiO_2), zirconia (ZrO_2) and ceria (CeO_2) are common supports for Ni catalysts. [3, 5] However, Ni has a tendency to oxidize unlike noble metals, which are often inert. [5] Noble metals are much more expensive but their inert abilities are of great interest. A noble metal that has gained interest is rhodium (Rh), which has shown promising results regarding high activity and selectivity for the methane. [4, 6] It has also shown higher stability than Ni, which makes it more resistant towards deactivation through sintering. [7]

1.1 Aim

In this study, the catalytic properties of Rh/CeO_2 for the Sabatier reaction will be explored, using different characterization methods and a fixed bed reactor. The effects the size of the Rh particles have on the catalytic properties will be the main focus. The obtained results will be compared with results from measurements done on $Rh/Ce_{1-x}Sm_xO_{2-\delta}$, $Rh/Ce_{1-x}Fe_xO_{2-\delta}$ and $Ce_{1-x}Rh_xO_{2-\delta}$ to see how dopants and the inclusion of Rh in the CeO_2 will affect the catalytic properties.

2 Theory

2.1 Sabatier reaction

2.1.1 Desired reaction

The Sabatier reaction is the methanation of CO_2, as shown below. [3]

$$\mathrm{CO_2} + 4\mathrm{H_2} \rightleftarrows \mathrm{CH_4} + 2\mathrm{H_2O} \qquad \Delta H = -165\ \mathrm{kJ\ mol^{-1}}$$

The reaction is exothermic and the CH_4 formation is thus favored by low temperatures as can be seen in Figure 1.

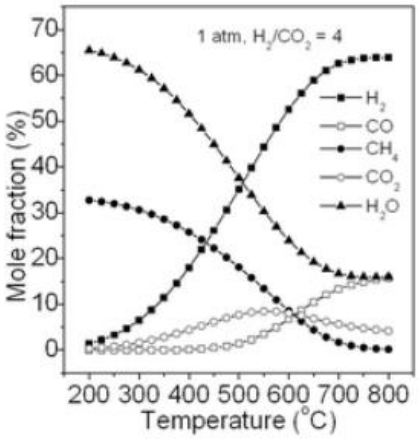

Figure 1: Product fraction of CO_2 methanation at equilibrium. [8]

The CH_4 formation is also dependent on the used pressure, since a lower pressure leads to a higher increase in entropy, as well as the H_2/CO_2 ratio. See Figure 2.

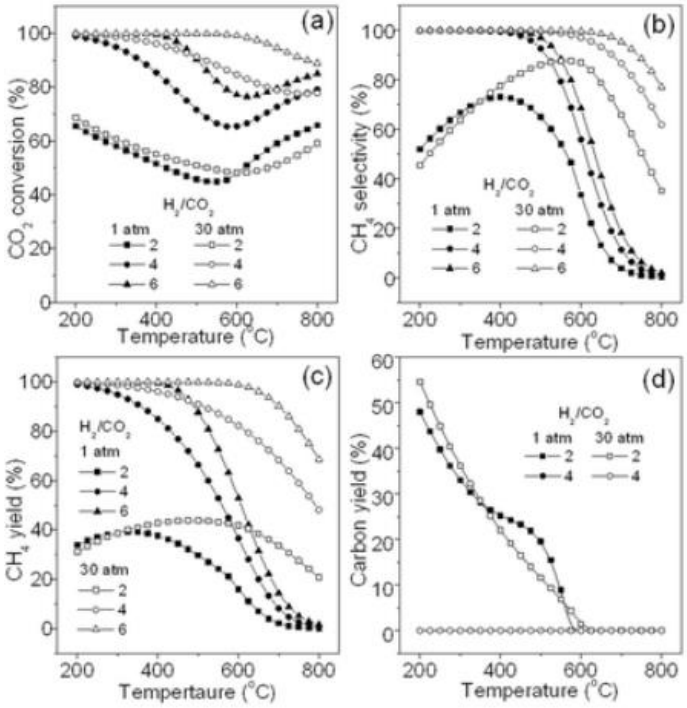

Figure 2: Effect of different H_2/CO_2 ratios on CO_2 methanation: (a) CO_2 conversion, (b) CH_4 selectivity, (c) CH_4 yield, and (d) carbon yield. [8]

The Sabatier reaction is then thermodynamically favorable at low temperatures due to the high negative change in enthalpy. However, the reaction rate is more favored by higher temperatures according to the Arrhenius equation:

$$k = Ae^{-\frac{E_A}{RT}} \quad (1)$$

CO_2 is a stable molecule which means that the activation energy will be high. As a result, even though the Sabatier reaction is thermodynamically favored, it will be kinetically controlled.

2.1.2 Side-reactions

One of the reasons for the decrease in CH_4 yield at elevated temperatures, approximately 500 °C, and lower pressures, is the slightly endothermic reversed water gas shift reaction (RWGSR) shown below. [3]

$$\mathrm{CO} + \mathrm{H_2O} \rightleftarrows \mathrm{CO_2} + \mathrm{H_2} \qquad \Delta H = -41\ \mathrm{kJ\ mol^{-1}}$$

At low temperatures the Sabatier reaction is more thermodynamically favored but enough energy must still be introduced to the system to start the reaction, as mentioned in previous section. However, an increase in temperature will eventually favor the RWGSR since $\Delta S \approx 0$ and for the Sabatier reaction $\Delta S < 0$. This is visualized in the Gibb's free energy shown below.

$$\Delta G = \Delta H - T\Delta S \quad (2)$$

Methanation of carbon monoxide (CO) may also occur even though this reaction, just like the Sabatier reaction, is favored by lower temperatures. [3]

$$\mathrm{CO} + 3\mathrm{H_2} \rightleftarrows \mathrm{CH_4} + \mathrm{H_2O} \qquad \Delta H = -206\ \mathrm{kJ\ mol^{-1}}$$

There might also be coke formation, which is one of the reasons for catalyst deactivation. The coke formation decreases with increasing temperature but so does the CO_2 methanation and too high temperature will also lead to RWGSR, see Figure 3.

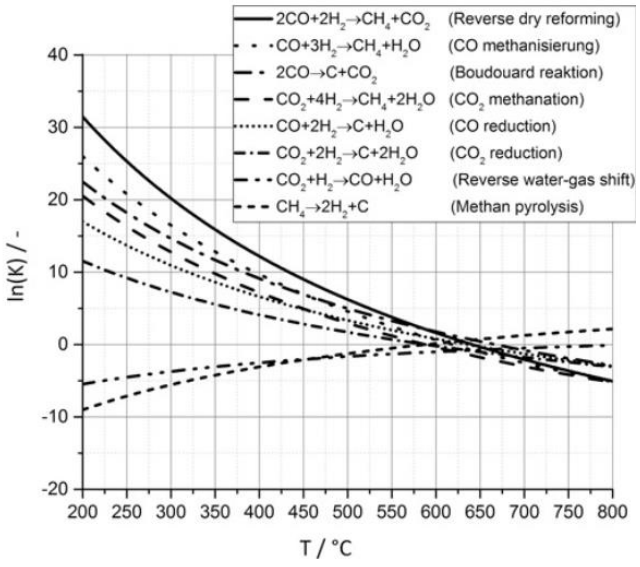

Figure 3: Natural logarithm of the equilibrium constants of possible reactions in the methanation process as a function of temperature. [5]

2.2 Catalysis

A catalyst is a material that facilitates a chemical reaction without itself being consumed. It lowers the activation energy for a chemical reaction by enabling new reaction pathways. By lowering the activation energy, a catalyst may increase the reaction rate and also change the selectivity of a reaction as shown in Figure 4 below.

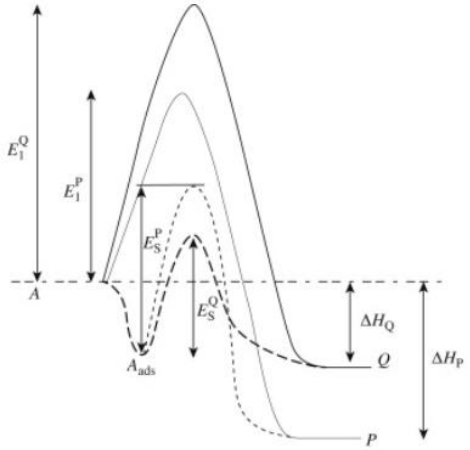

Figure 4: Schematic representation of the energetics of two parallel reactions A → P and A → Q, showing that a catalyst can change the selectivity. [9]

As seen in Figure 4, the introduction of a catalyst turns product Q from the least kinetically favored product to the most favored. This despite the fact that product P remains the thermodynamically favored product.

Catalysis can later be divided into two groups: homogeneous and heterogeneous catalysis. In homogeneous catalysis the catalyst, reactants and products are in the same phase while in heterogeneous catalysis the catalyst is in another phase than the reactants and products. [8] Unlike homogeneous catalysis, heterogeneous catalysis allows for easier separation and recovery of the catalyst as well as higher thermal stability, but with the drawback of a generally lower selectivity.

2.2.1 Supported catalysts

Within catalysis, a big surface area to volume ratio is desired since the catalytic activity increases and more of the catalytic material is utilized. However, this also makes the catalyst less stable and more prone to e.g. sintering, which decreases the catalytic properties. One way to enable a high surface area to volume ratio, while limiting the sintering, is to use so called supported catalysts. These catalysts are a version of heterogeneous catalysts where the metal particles are fixed onto a support, usually an oxide with a high melting temperature since it makes it stable under most reaction conditions. [9] This support can be inert as well as contribute to the selectivity and activity of the catalyst. [10] A porous support structure is desirable since it provides a high surface area which allows for more metal particles on the surface and thus a higher catalytic activity. However, one must consider the size of the pores so that the reactants and product, as well as the active metal, may reach into them. [9]

2.2.2 Doped support material

By doping the support with different promoters, the stability of the material can be increased and it will thus be more resistant towards sintering since movements will be limited due to the promoters acting as anchors. [10] Dopants also have the possibility to increase the selectivity of a catalyst, as well as form more active sites which increases the reaction rate.

Commonly, the dopants are electropositive and allow for easier electron transfer between the catalyst and the reactants. [11]

2.2.3 Deactivation of catalysts

An active material with a high surface area to volume ratio is desirable within catalysis, as mentioned earlier. However, a smaller particle, and thus a tighter curvature, also means a higher total surface energy. Since nature strives to minimize this energy, the catalyst will suffer from sintering where small particles move together to form bigger particles and thus decrease the total surface energy. This is not desirable since it means that the surface area and thus the activity of the catalyst will decrease. By using a supported catalyst this problem might be minimized, but not avoided, since the metal particles are fixed in place on a stable support material. [9] The risk of sintering increases with increasing temperature [5] but by using a higher calcination temperature during the synthesis of the catalyst compared to the reactor temperature, the sintering can be more limited.

Fouling is another way of deactivation where the active sites, or the pores where the active sites are located, are physically blocked by depositions of e.g. coke.

2.3 Synthesis of the catalyst

2.3.1 Dry impregnation

This method is very common for the synthesis of heterogeneous catalysts due to its simplicity, low cost and low amount of waste. [12] A precursor is dissolved in a solution and has the same volume as the effective pore volume of the support material, to which the solvent is being added. Capillary forces then draw the solvent into the pores, compared to wet impregnation where a bigger volume of solvent is used and the impregnation is diffusion controlled. [13] The dry impregnation makes it easy to control the weight percentage of added metal but with the drawback that it is hard to get them evenly distributed over/within the support. [9]

2.3.2 Freeze-drying

After the impregnation the solvent must be removed. Within the industry the conventional method is heating, sometimes together with vacuum drying. However, when the solvent evaporates it pulls the solid particles along with it towards the surface which causes the particles to form bigger clusters and potentially block pores. This is a disadvantage since active surface area is lost and only parts of the support material will be used.

Freeze-drying is one way to circumvent this problem. The solvent will then evaporate by sublimation, or in other words, go from solid phase directly to gas phase without first

going through the liquid phase. [14] In this way the metal particles are able to stay in a well distributed way on the support material even during drying.

2.3.3 Calcination

Calcination is a thermal treatment used as a way of purifying the sample by removing volatile constituents at high temperatures so that only the desired metal particles remain on the support material. It also stabilizes the catalyst by setting the particles in place and decreases the risk of deactivation through sintering, as long as the calcination temperature is higher than the temperature later used during the catalyzed reaction. However, increased calcination temperature comes with the drawback of decreased surface area since more of the material is fused together, as well as a decrease in catalytic activity. [9]

2.4 Analysis methods

2.4.1 BET – Brunauer-Emmett-Teller theory

The main idea of this analysis method is to estimate the specific surface area through the amount of adsorbed nitrogen (N_2) molecules on the material at low temperature. The amount of N_2 molecules present in the system is controlled by careful adjustments of the pressure. It is assumed that the N_2 acts as an ideal gas and forms uniform layers on the surface. Out of these layers, closest to the solid surface, is a monolayer with higher enthalpy of adsorption and then there are additional multilayers of lower enthalpy of adsorption. The enthalpy of adsorption is assumed to be constant throughout the multilayers.

The BET theory results in Equation 1 below:

$$V_{ads} = \frac{V_{\mathrm{m}} cP}{(P^0 - P)\{1 + \frac{(c-1)P}{P^0}\}} \tag{1}$$

where V_{ads} is the volume of adsorbate, V_m is the volume required to give a monolayer of adsorbed molecules, P is the measured pressure of the gas, P^0 is the saturated vapor pressure of the gas at the temperature of adsorption and c is a constant. [15] This equation can in turn be linearized as shown below:

$$\frac{P}{V_{\mathrm{ads}}(P^0 - P)} = \frac{1}{V_{\mathrm{m}} c} + \frac{c-1}{V_{\mathrm{m}} c}\frac{P}{P^0} \tag{2}$$

Plotting the left side against P/P^0 will result in $1/V_m c$ at the y-axis interception and $(c-1)/(V_m c)$ as the slope, which will give the value of V_m and c. The specific surface area is then calculated as:

$$S_{\mathrm{BET}} = \frac{V_{\mathrm{m}} N s}{V a} \tag{3}$$

where N is Avogadro's number, s is the adsorption cross section of the adsorbate, V is the molar volume of the adsorbate and a is the mass of the solid sample.

2.4.2 XRF – X-ray fluorescence

When X-rays of wavelengths corresponding to the ionization energy of the atom of interest are aimed at a sample, an electron from the inner levels will be knocked out. An

electron from the outer levels will then move to fill this electron hole, emitting energy as X-rays in the process. This emitted energy is characteristic for each element and is used to analyze the constituents of the sample and estimate their respective amounts. [16] This process is visualized in Figure 5 below.

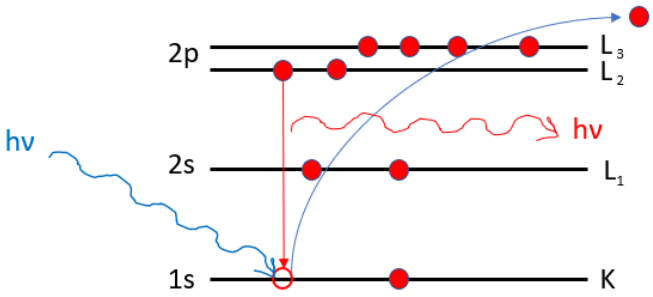

Figure 5: Illustration of the principle of XRF.

2.4.3 CO chemisorption

Gases may adsorb onto different materials in two ways: chemisorption and physisorption. Chemisorption is much stronger since a chemical bond is formed between the gas and the solid, compared to physisorption where the interactions are based on the weaker van der Waals forces. [17] This makes a chemisorbed layer harder to remove than a physiosorbed layer. Additionally, chemisorption can only form monolayers since the gas molecules must be in direct contact with the solid surface. In contrast, multilayers are able to form through physisorption, both on top of the chemisorbed monolayer as well as on the rest of the support. [18]

In this experiment it is assumed that all Rh surface acts as an active site. The CO chemisorption can then be used to estimate the average size of the active sites and the dispersion, which is the percentage of the present active atoms that are surface atoms and thus available for chemisorption. The reason for CO to be utilized as adsorbate is that it has a low probability of adsorbing onto the CeO_2, which makes it possible to only study the Rh.

This experiment will result in a chemisorbed monolayer and several physisorbed multilayers. The physisorbed CO will then be removed so that only the chemisorbed monolayer remains and then the CO molecules will be added again through physisorption. It is then possible to subtract the obtained diagram of chemisorption + physisorption with the one obtained from only physisorption to get the data for the chemisorbed monolayer.

The average size of a hemispherical active site is calculated as shown below: [19]

$$D = \frac{6}{\rho_{\mathrm{Rh}} * A_{\mathrm{m}}} \tag{4}$$

where ρ_{Rh} is the density of Rh [kg/m^3] and A_m is the active surface area per unit mass of metal [m^2/g Rh]. The density is already known but the A_m can be calculated as:

$$A_{\mathrm{m}} = \frac{A_{\mathrm{A}}}{m_{\mathrm{m}}} \tag{5}$$

where A_A is the specific active surface area [m^2] and m_m is the mass of Rh [g]. Here, the weight percentage of Rh in the sample is known, as well as the mass of the sample, which makes the mass of Rh known. A_A can be calculated as:

$$A_{\mathrm{A}} = A_{\mathrm{Rh}} * N_{\mathrm{Rh}} \tag{6}$$

where A_{Rh} is the area occupied by one Rh atom and N_{Rh} is the number of Rh surface atoms. A_{Rh} can be found in literature and the number of Rh surface atoms can be calculated as:

$$N_{\mathrm{Rh}} = F * N_{\mathrm{CO}} = F * N_{\mathrm{A}} \frac{PV}{RT} \tag{7}$$

where N_{CO} is the number of chemisorbed CO molecules estimated by the experiment through the use of the ideal gas law and Avogadro's number and F is a stoichiometric factor telling how many Rh atoms one CO molecules binds to. It is here assumed to be 1. All other parameters in Equation 7 are known, with only the pressure as the changing variable.

2.4.4 DRIFTS – Diffuse reflectance infrared Fourier transform spectroscopy

This method provides information regarding both chemical and structural properties. [20] The sample does not need any particular preparation and does not have to be transparent which makes this method desirable. However, if the catalyst has a too high absorption, then it can be mixed with an IR-transparent material such as potassium bromide (KBr).

Incoming IR-radiation of known energy will be reflected through diffusive scattering and the loss in intensity of the incoming light, which is due to certain wavelengths corresponding to the vibration energies of different bonds, will be detected. [21] This method can thus be used to study what species that are formed on the surface of the catalyst during the CO_2 methanation and how these species are bonded to the catalyst.

2.4.5 Reactor measurements

Overall, a low amount of sample and a low conversion is desirable for these measurements due to three main reasons. The first one being that the pressure drop when going from 5 mol to 3 mol, see the Sabatier reaction shown in the introduction, can be negligible. Secondly, the temperature increase caused by the heat released from the exothermic reaction may also be negligible, thus assuming an isothermic system. The third reason is that the reaction is kinetically controlled, thus not controlled by mass transport.

3 Methods

The used chemicals for the upcoming part are as follows: CeO_2 (Sigma Aldrich), rhodium nitrate ($Rh(NO_3)_3$) with 36 wt% Rh basis (Sigma Aldrich) and KBr (Sigma Aldrich).

3.1 Dry impregnation

3.1.1 Preparation of the CeO_2

In order to obtain a powder size in the range 40-80 µm, CeO_2 powder was pressed into pellets at 10 tons pressure (Specac) previous to calcination. Both CeO_2 powder and CeO_2 pellets were then calcinated for one hour at 600 °C with a temperature ramp of 5 °C/min. The powder was then sieved to see if the right size had been obtained while the pellets were grinded and sieved to the right size. A new and bigger batch of the pelleted CeO_2 was made for the rest of the experiments after a BET measurement (drying at 250 °C for 4h) had confirmed that the specific surface area was high enough.

3.1.2 Effective pore volume

The effective pore volume of CeO_2 was determined by adding milliQ-water dropwise to ~1 g of CeO_2 on a scale until the maximum absorption point was reach and it turned to liquid. The mass of added milliQ-water was noted and the effective pore volume was calculated according to:

$$V_{\text{pore}} = \frac{m}{\rho} * 10^6 \tag{8}$$

where *m* is the mass of the added water [kg], *ρ* is the density of milliQ-water [998 kg/m^3] and 10^6 is to convert the volume to milliliters. The calculated volume was then divided with the exact mass of the CeO_2. The effective pore volume was then estimated to 0.520 ml/g CeO_2.

3.1.3 Precursor calculations

The amount of precursor needed for the desired weight percentages of Rh on CeO_2 was calculated as:

$$m_{\text{Rh(NO}_3)_3} = \frac{x}{0.36} \tag{9}$$

where *0.36* is for the weight percentage of Rh in the $Rh(NO_3)_3$ precursor and *x* is the amount of Rh that needs to be added to 0.80 g CeO_2 to get the desired weight percentages of Rh on the CeO_2. *X* is calculated as below:

$$\frac{x}{m_{\text{CeO}_2}+x} = y \Rightarrow x = \frac{m_{\text{CeO}_2} * y}{1-y} \tag{10}$$

where *y* is the desired weight percentage, in decimal form, of Rh on CeO_2.

The volume milliQ-water, in which the precursor will be dissolved, was calculated as:

$$V = V_{\text{pore}} * m_{\text{CeO}_2} \tag{11}$$

where V_{pore} is the effective pore volume calculated in Equation 8 and m_{CeO_2} is the mass of CeO_2 used, in this case 0.80 g.

Table 1 shows a compilation of the calculated amounts that are needed for the desired weight percentages: 1, 2 and 3. The samples are referred to as Rh1, Rh2 and Rh3, respectively. All amounts were prepared with additional 5 % to have some margin during the impregnation.

Table 1: Compilation of calculated amounts material needed for the dry impregnation to obtain the desired weight percentages of Rh on CeO_2.

Sample	**Rh [g]**	**CeO_2 [g]**	**$Rh(NO_3)_3$ [g]**	**milliQ-water [ml]**
Rh1	0.0081	0.80	0.0225+0.0236	0.416+0.437
Rh2	0.0163	0.80	0.0453+0.0476	0.416+0.437
Rh3	0.0247	0.80	0.0686+0.0720	0.416+0.437

3.1.4 Impregnation

The calculated amount of $Rh(NO_3)_3$ precursor for each weight percentage was dissolved in 0.437 ml milliQ-water. However, it was discovered that the precursor easily absorbed water from the surrounding air, which made the weights less accurate. The lids for each vial were then quickly closed after each addition of sample to try to minimize the absorption.

A volume of 0.416 ml of each solution was added to ~0.80 g CeO_2 each. All samples were placed in their own vials and sealed with aluminium foil with a few holes poked into it. The samples were then placed in a freeze-dryer (ScanVac CoolSafe), after being held in liquid nitrogen until no boiling occurred. The samples were left in the freeze-dryer for ~21 h.

Note: The samples turned wet after the vials were tapped against the table to get the samples down to the bottom of the vials before the freeze-drying. The samples quickly started to form two layers, with the wet CeO_2 at the bottom and solution with a high Rh concentration on top. Each sample was stirred and quickly put into the liquid nitrogen to avoid the sample from phase separating again. A comparison between the wet samples and samples with the right consistency is shown in Figure 6:

Figure 6: Left: A batch of samples with the right consistency before freeze-drying. Right: The obtained samples before freeze-drying.

3.1.5 Calcination

The samples were removed from the freeze-dryer and placed in separate crucibles, which were placed in the calcination oven. They were then calcinated at 500 °C for one hour, with a temperature ramp of 5 °C/min.

3.2 BET-measurements

The samples were placed in separate sample tubes and their respective masses were noted for later use.

The samples were dried in two different ways: with a N_2 flow at 250 °C, with a temperature increase of 20 °C/min, for either 4 h or overnight. Both these methods resulted in a negative mass change. The beakers were then connected to the BET equipment (Micromeritics TriStar 3000) and the measurement was started.

3.3 XRF

The samples were added to separate cups. The mass of each of the added samples was noted and the XRF was then run (PANalytical Axios XRF spectrometer).

3.4 CO chemisorption

Each sample was placed between two pieces of folded quartz wool in a u-tube. The mass of the sample was noted and the u-tube was mounted in the CO chemisorption apparatus (Micromeritics ASAP 2020 Plus). The pre-treatments shown below were then run prior to the CO chemisorption.

Table 2: First pre-treatment program with O_2 and H_2.

Task	**Temperature [°C]**	**Time [min]**
O_2 flow	350	30
Evacuation	350	15
H_2 flow	350	30
Evacuation	350	10
Evacuation	35	60
Leak test	35	1
Evacuation	35	10

Table 3: Second pre-treatment program with pre-adsorption of CO_2 at low temperature after H_2 flow.

Task	**Temperature [°C]**	**Time [min]**
O_2 flow	350	30
Evacuation	350	15
H_2 flow	350	30
Evacuation	350	10
Evacuation	35	15
CO_2 flow	35	10
Evacuation	35	60
Leak test	35	1
Evacuation	35	10

Table 4: Third pre-treatment program with pre-adsorption of CO_2 at high temperature before H_2 flow.

Task	**Temperature [°C]**	**Time [min]**
O_2 flow	350	30
Evacuation	350	15
CO_2 flow	350	10
Evacuation	350	15
H_2 flow	350	30
Evacuation	350	10
Evacuation	35	60
Leak test	35	1
Evacuation	35	10

A fourth pre-treatment was run for Rh1 to see if, by chance, a temperature change in the CO_2 flow would lead to a different dispersion and particle size when CO_2 was flowed last.

Table 5: Fourth pre-treatment program with pre-adsorption of CO_2 at high temperature after the H_2 flow.

Task	**Temperature [°C]**	**Time [min]**
O_2 flow	350	30
Evacuation	350	15
H_2 flow	350	30
Evacuation	350	15
CO_2 flow	350	10
Evacuation	350	10
Evacuation	35	60
Leak test	35	1
Evacuation	35	10

3.5 DRIFTS

Each sample was mixed separately with KBr of the same grain size (40-80 µm) to obtain a total of approximately 5 wt% of sample in the mixture. Two filters were placed at the bottom of the cup in the apparatus and the sample was added on top of the filters and the surface was then flattened, using a scraper. The DRIFTS study was conducted using a BRUKER Vertex 80v spectrometer equipped with a nitrogen cooled MCT detector and a high-temperature stainless steel reaction cell (Harrick Praying Mantis™ high temperature reaction chamber) with KBr windows. The temperature of the sample holder was measured by a thermocouple (type K) and controlled by a PID regulator (Eurotherm).

The pre-treatments for the DRIFTS were then run in the same manner and order as during the CO chemisorption, see Table 2-5, but using a pure argon (Ar) flow instead of evacuation. The volumetric percentages of O_2, H_2, CO_2 and CO were 20, 50, 50 and 50, respectively. Pure Ar was used as carrier gas and kept the total flow at 100 ml/min. A new set of measurements were later made under the reaction conditions used in the fixed bed reactor, described in following section. However, for the DRIFTS measurements the H_2 and CO_2 flows were 4 and 1 vol% of the total flow, respectively.

3.6 Reactor measurements

A known amount of sample was added to the reactor between two pieces of folded quartz wool. It was then connected to the system, equipped with a mass spectrometer, and wrapped in isolating fabric.

The measurement was then run with a total flow of 150 ml/min at 150, 250, 350 and 400 °C, with Ar as the carrier gas. A constant CO_2 flow of 0.5 vol% of the total flow was used and at each temperature there were three H_2 pulses (10 min) followed by a longer H_2 pulse (120 min), with the purpose of the longer pulse to reach a steady state. The H_2 flow was 2 vol% of the total flow, thus leading to a H_2/CO_2 ratio of 4.

To minimize the risk of fluctuations in the data caused by fluctuations in the carrier gas Ar, the obtained ion current was normalized using the Ar flow, which ion current in turn was corrected by dividing it with the volume percentage of Ar in the total flow:

$$I_{Ar,corr} = \frac{I_{Ar}}{y_{Ar}} \tag{12}$$

where I_{Ar} is the obtained ion current for Ar [A] and y_{Ar} is the volume percentage, in decimal form, of Ar in the total flow.

The reaction rate, based on the consumption of CO_2, was then calculated for each temperature and sample as described below:

The CO_2 conversion at temperature j was calculated as

$$x_j = \frac{\dot{V}_{j,0} - \dot{V}_{j,ss}}{\dot{V}_{j,0}} \tag{13}$$

where $\dot{V}_{j,0}$ is the volumetric flow [ml/min] just before the first H_2 pulse and $\dot{V}_{j,ss}$ is the volumetric flow [ml/min] at steady-state at temperature j. Each flow was previously in turn calculated as

$$\dot{V}_{CO_2} = I * z_{co_2} \tag{14}$$

where I is the obtained ion current [A] for CO_2, using a mean value of 5 different points, and z_{CO2} is a previously obtained calibration factor of 0.0095494 ml/(min*A).

The reaction rate was then calculated using Equation 15:

$$r_{j,CO_2} = F_{0,tot} * x_j \tag{15}$$

where $F_{0,tot}$ is the initial molar flow of CO_2 [mol/min], which was calculated using

$$F_{0,tot} = \frac{P\dot{V}}{RT} \tag{16}$$

where P is the pressure [1 atm], $\dot{V}$ is the volumetric flow of CO_2 [$7.5*10^{-7}$ m^3/min], R is the gas constant [8.314 J/K*mol] and T is the temperature [273.15 K] (the values are the flow controllers' manufacturer Bronkhorst's normal conditions).

For easier comparison of the results, the reaction rates were normalized to [mol/(min*mg Rh)] and [mol/(min*m^2 Rh)] by using Equation 17 & 18, respectively

$$r_{j,CO_2(mg\ Rh)} = \frac{r_{\mathrm{j,CO_2}}}{m_{\mathrm{Rh}}} \tag{17}$$

$$r_{j,CO_2(m^2\ Rh)} = \frac{r_{j,CO_2}}{A_{Rh}} \tag{18}$$

where m_{Rh} is the mass [mg] of Rh in each sample and A_{Rh} is the area [m^2] of Rh in each sample.

The selectivity for CH_4 was calculated for each temperature and sample as described below:

The volumetric flow of formed CH_4 [ml/min] at each temperature was calculated as

$$\dot{V}_{j,CH_4} = \dot{V}_{CH_4,ss} - \dot{V}_{CH_4,0} \tag{19}$$

where $\dot{V}_{CH_4,ss}$ is the volumetric flow [ml/min] at steady-state at temperature j and $\dot{V}_{CH_4,0}$ is the volumetric flow [ml/min] just before the first H_2 pulse. Each flow was in turn previously calculated as

$$\dot{V}_{CH_4} = I * z_{CH_4} \tag{20}$$

where I is the obtained ion current [A] for CH_4, using a mean value of 5 different points, and z_{CH4} is a previously obtained calibration factor of 0.00034557 ml/(min*A).

The molar flow of formed CH_4 [mol/min] at each temperature was then calculated as

$$F_{j,CH_4} = \frac{P\dot{V}_{j,CH_4}}{RT} \tag{21}$$

where P is the pressure [1 atm], $\dot{V}$ is the volumetric flow of CH_4 [m^3/min] from Equation 19, R is the gas constant [8.314 J/K*mol] and T is the temperature [273.15 K] (the values are the flow controllers' manufacturer Bronkhorst's normal conditions).

The molar flow was then divided by the mass Rh in each sample to obtain the same unit as for the reaction rate of CO_2, [mol/(min*mg Rh)]:

$$r_{j,CH_4(mg\ Rh)} = \frac{F_{j,CH_4}}{m_{Rh}} \tag{22}$$

The selectivity for CH_4 [%] at each temperature was then calculated as

$$S_j = \frac{r_{j,CH_4(mg\ Rh)}}{r_{j,CO_2(mg\ Rh)}} * 100 \tag{23}$$

where the factor 100 is used to convert the unit to %.

4 Results/Discussion

4.1 Synthesis

The three synthesized Rh/CeO_2 samples are presented in Figure 7.

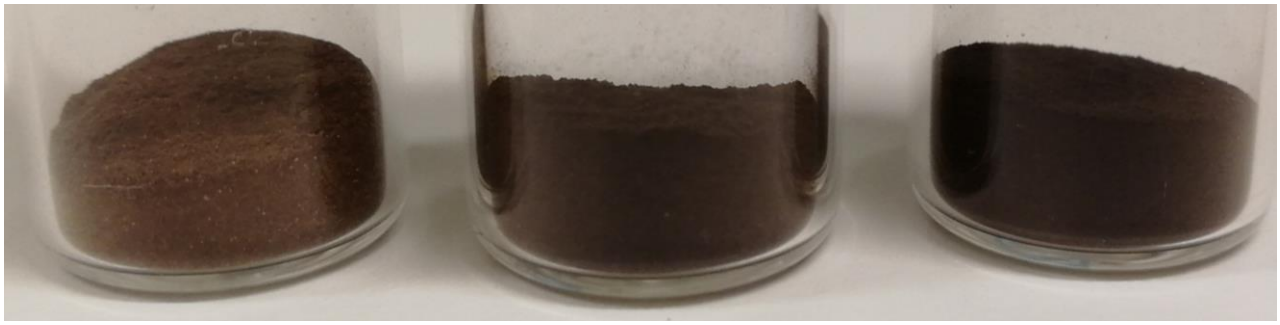

Figure 7: The synthesized Rh/CeO_2 samples with, from the left: Rh1, Rh2 and Rh3.

As seen in Figure 7, several small light spots are present in Rh1 which probably are an indication of non-impregnated CeO_2 particles. This could be due to that the samples turned wet and formed different layers, as was shown in Figure 6. If the layers had not formed then it would stand to reason that all CeO_2 should have been impregnated since wet impregnation leads to a more evenly distributed impregnation than dry impregnation, as mentioned in Section 2.3.1. One reason for the samples to turn wet could be that bubbles were formed during the measurement of the effective pore volume so that more liquid could be added before it turned wet.

4.2 XRF

The estimated weight percentages of Rh on CeO_2 from the XRF are presented in Table 6 below.

Table 6: Estimated weight percentages of Rh in the samples.

Sample	**Aimed wt% Rh/CeO_2**	**Measured wt% Rh/CeO_2**
Rh1	1	1.0
Rh2	2	1.8
Rh3	3	2.5

As can be seen, the error increased with increasing weight percentage. The absorption of water from the air was probably the main contribution considering that it took longer time to weight a larger amount of precursor.

In Section 4.1, Figure 7, it was shown that Rh1 was not completely impregnated. This does not however seem to affect the obtained weight percentage of Rh on the sample.

4.3 BET

Table 7 below shows the specific surface area for both the pure CeO_2 and the impregnated samples.

Table 7: Specific surface area for all impregnated samples and the pure CeO_2 that was used for each batch of impregnated samples.

Sample	**S_{BET} [m^2/g sample] (4 h drying)**	**S_{BET} [m^2/g sample] (drying overnight)**
CeO_2	111[1]	---
Rh1	115	129
Rh2	118	133
Rh3	118	123

1. *The small test batch of pelleted CeO_2 calcinated at 600 °C (not the same that was used for the impregnated samples due to the sample being lost before the BET could be made).*

A longer drying time increases the observed specific surface area of the catalysts, as shown in Table 7, which is due to more water being evaporated. It then stands to reason that 4 h of drying at 250 °C is not enough to remove all water from the sample, thus making the results less reliable.

In general, a decrease in specific surface area could mean that bigger Rh particles are formed on the CeO_2 so that the area/mass ratio decreases. This theory can be verified by studying the results from the CO chemisorption. However, the BET results show no clear trend of higher Rh load leading to a smaller specific surface area. It could be due to faulty drying, error in the measurement or that the Rh particles on Rh2 in fact are smaller and more distributed than on Rh1 and Rh3. Even here the results from the CO chemisorption should be able to cast some light over the reason.

The specific surface area seems to increase when impregnating CeO_2 with Rh. Even though the CeO_2 represented in Table 7 is not the same CeO_2 that was used for the second batch, it should theoretically have the same specific surface area since they were synthesized the same way. The assumption that the CeO_2 used for the Rh/CeO_2 can be represented by the small test batch described in Section 3.1.1 should then be fairly accurate.

4.4 CO chemisorption

The dispersion and mean Rh particle size for all samples are presented in Table 8 below. A dispersion of 100 % means that all the Rh is occupying the support surface as individual atoms.

Table 8: Summary of the dispersions, crystallite sizes (hemispheres), CO uptakes and metallic areas for all Rh/CeO_2 samples.

Sample	**Dispersion [%]**	**Diameter [nm]**	**CO uptake [µmol/g sample]**	**Rh area [m^2/g sample]**
Pre-treatment: O_2, H_2				
CeO_2	~2[1]	---	---	---
Rh1	127	0.86	123	5.61
Rh2	94	1.17	164	7.41
Rh3	87	1.26	211	9.60
Pre-treatment: O_2, H_2, CO_2				
Rh1	48	2.29	47	2.11
Rh2	48	2.30	84	3.78
Rh3	40	2.77	97	4.37
Pre-treatment: O_2, CO_2, H_2				
Rh1	109	1.01	106	4.79
Rh2	79	1.40	138	6.23
Rh3	68	1.62	165	7.45
Pre-treatment: O_2, H_2 (repeat)				
Rh2	91[2]	1.21	159	7.22
Pre-treatment: O_2, H_2, CO_2 (HT)				
Rh1	44[3]	2.50	43	1.94

1. *Used setting: 3 wt% Rh to see if pure CeO_2 might adsorb CO.*
2. *A second O_2, H_2 pre-treatment that was made after the measurement with O_2, H_2, CO_2 pre-treatment to see if the carbonates were easily removed.*
3. *The fourth pre-treatment with CO_2 flow at high temperature.*

The Rh particle diameter shows a trend of increasing with increasing Rh load for all pre-treatments. However, for the O_2, H_2 pre-treatment, Rh1 has a dispersion over 100 %. The results for pure CeO_2, using the same pre-treatment, show that the support is active, although not enough to contribute to this high dispersion. It is not unthinkable that a small Rh particle size could affect the CeO_2 at the interface between the particle and the support, making it act as new active sites. However, the fact that the dispersion is way over 100 % and quite high for the two other impregnated samples as well, makes the O_2, H_2 pre-treatment less correct for the estimation of the mean particle size.

A distinct change in the estimated particle size can be seen when the O_2, H_2, CO_2 pre-treatment is used. One reason could be the oxidation of the metallic Rh, RhO_x, caused by the CO_2. The number of available Rh sites would then be decreased. Additionally, the number of available Rh sites may also decrease due to dissociatively adsorbed CO_2, which forms a CO that can adsorb onto the Rh before the real CO chemisorption measurement is started. Lastly, the CeO_2, which showed evidence of activity, could also be affected due to the formation of carbonates (CO_3^-) on its surface. The carbonate formation is easier for CO_2 than CO because of the extra oxygen and the low temperature of the CO_2 flow allows for all of the carbonates to remain there. However, the O_2, H_2 pre-treatment run between the two different CO_2 pre-treatments for Rh2 seems to be able to remove most of the adsorbed CO and carbonates, as well as reduce the formed RhO_x back to metallic Rh.

The O_2, CO_2, H_2 pre-treatment shows a higher estimated dispersion compared to the O_2, H_2, CO_2 pre-treatment. The formed RhO_x from the O_2 flow and the CeO_2 provide oxygen for the CO_2 to form carbonates on the two surfaces. Also, the metallic Rh can adsorb CO through dissociative adsorption of CO_2, as mentioned earlier. However, elevated temperatures and the following H_2 flow should remove the adsorbed CO and reduce the RhO_x back to metallic Rh, as well as remove some of the carbonates. This could indicate that the O_2, CO_2, H_2 pre-treatment results in a more realistic estimated dispersion. However, even here Rh1 has a dispersion over 100 % which, as discussed earlier, could be due to sites being formed in the metal-support interface.

The increased temperature for the CO_2 flow, shown last in Table 8, does not seem to have a significant effect compared to the corresponding pre-treatment with CO_2 flow at low temperature. However, it cannot be said for certain that the small decrease in dispersion is not due to an increased number of carbonates and a higher degree of oxidation.

Another interesting observation during these measurements was the easy re-oxidation of reduced CeO_2. Figure 8 below shows the reduced CeO_2 before and after being exposed to air at room temperature for only a few seconds. The impregnated samples did not oxidize as easily.

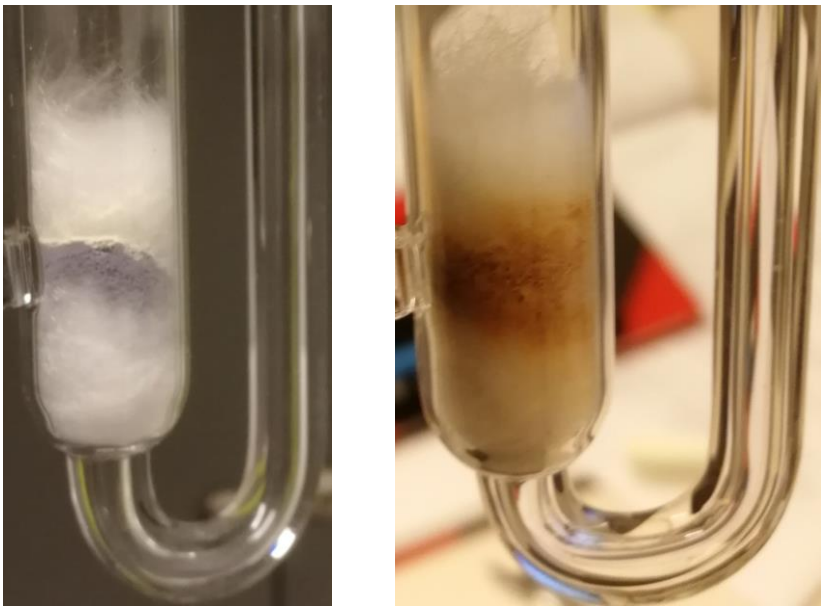

Figure 8: Pictures of partially reduced CeO_2 (left) and the same sample, now starting to re-oxidize seconds after being exposed to air at room temperature (right).

4.4.1 DRIFTS – CO chemisorption

The DRIFTS spectra of all samples, pretreated with O_2 and H_2, during ongoing CO flow are shown in Figure 9 below.

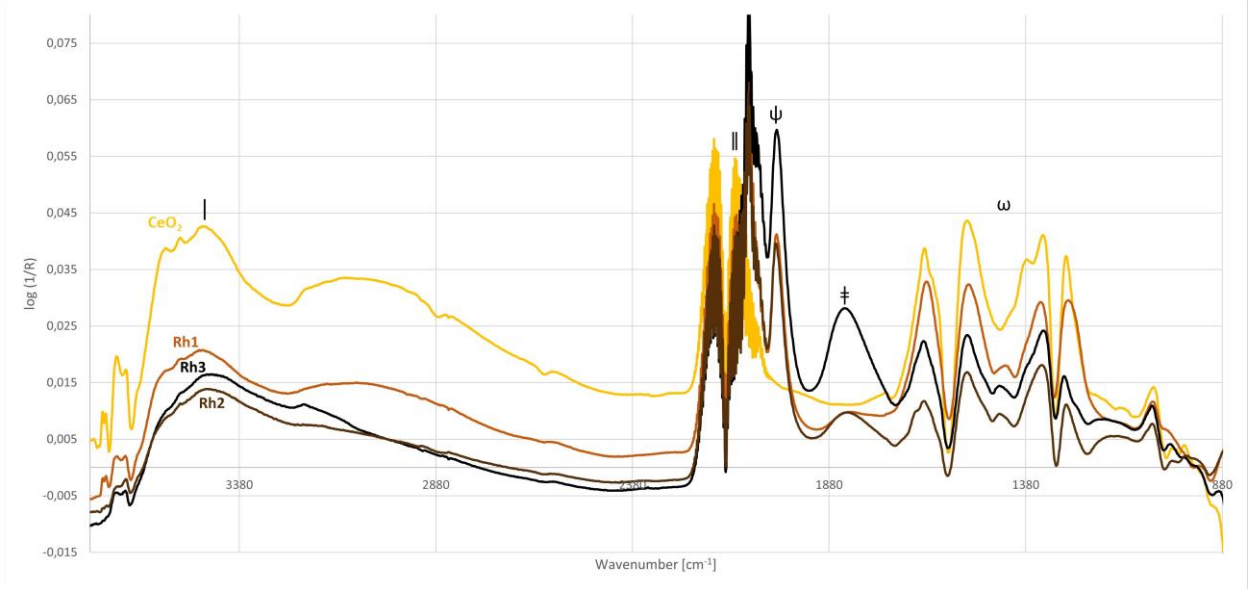

Figure 9: DRIFTS spectra of all samples, pre-treated with O_2 and H_2, during exposure to a flow of 50 vol% CO at 35 °C.

Table 9 shows the observed peaks and wavenumbers along with the corresponding species for each.

Table 9: IR absorption bands discussed in this study.

Peak	**Wavenumber [cm^{-1}]**	**Species**	**Ref.**
I	3000-3700	Hydroxyl region	[22]
II	2100-2200	Gaseous CO, with its corresponding peak on the left	[23]
χ	2349	Gaseous CO_2, with its two corresponding double peaks around 3550-3750 cm^{-1}	[22, 24, 25]
ψ	2020	Linearly bonded CO on Rh, with its corresponding peak on the left	[24, 26, 27]
ǂ	1750-1900	Bridge-bonded CO on Rh	[24, 26-28]
*	1720	Bridge-bonded CO on Rh-CeO_2 interface	[6]
ω	1200-1600	Carbonate-like species	[24, 26, 27]

The wide area in the left part of the spectrum corresponds to OH groups, which shows the presence of water, but also eventual Rh-OH and CeO_2-OH on the surface. When observing the absorption for CeO_2, there are two sharp peaks in the approximate interval of 2100-2200 cm^{-1} present. These show the gaseous CO. However, for the impregnated samples there is a peak around 2020 cm^{-1}, which is characteristic for linearly bound CO to Rh. Additionally, another peak is present around the interval 1750-1900 cm^{-1}, which is characteristic for bridge-bonded CO on Rh.

The peaks in the region 1200-1600 cm^{-1} show the presence of carbonates on the catalysts. By comparing the intensity ratio between gaseous CO and these peaks for all samples, it can be seen that the one for pure CeO_2 is relatively high. This could be an indication of CeO_2 being able to adsorb CO as well.

Figure 10 below shows the same samples, after the gaseous CO has been removed and the samples have been exposed to an Ar flow for 30 min.

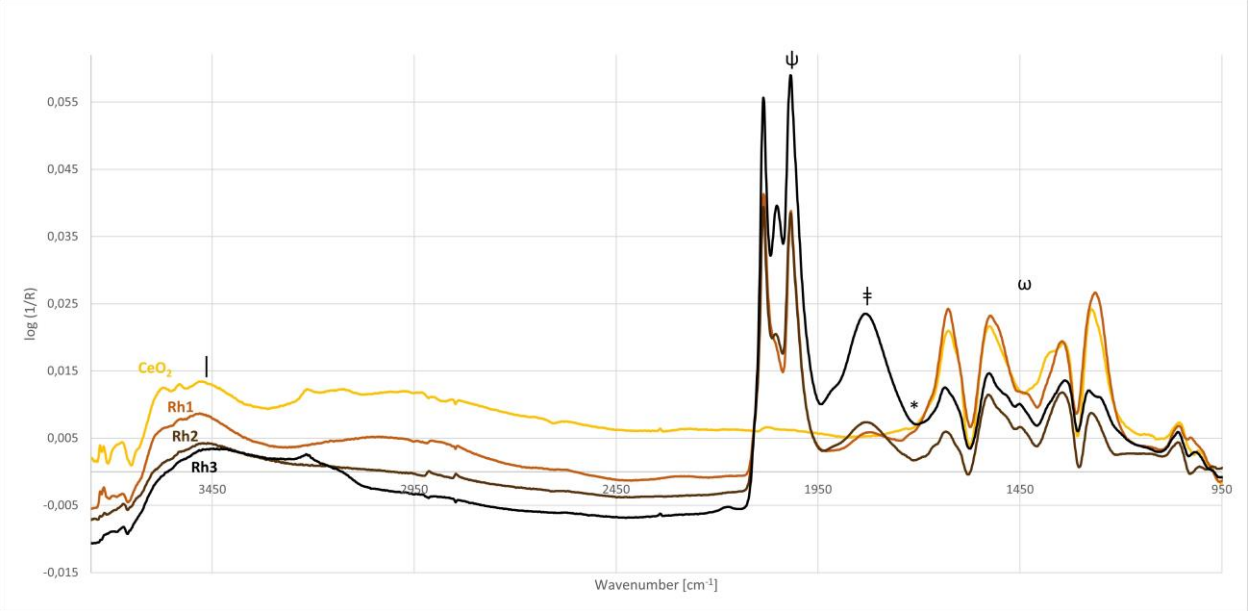

Figure 10: DRIFTS spectra of all samples shown in Figure 9 after a pure Ar flow at 35 °C for 30 min.

The two peaks for gaseous CO have disappeared since the Ar flow has removed all CO from the system, but the 2020 cm^{-1} peak is still present, along with its second peak, due to the strong chemisorption. Another peak is now present on its left. This peak is the second CO peak for adsorbed CO and was present even in Figure 9, though hidden beneath the stronger peaks of gaseous CO. However, a new peak of unknown origin can be seen between the two CO peaks with increasing Rh load.

The peak for bridge-bonded CO on Rh is also present. This means that the assumption that all CO binds linearly to Rh is inaccurate. The stoichiometric factor *F* in Equation 7, see Section 2.4.3, should then have a value between 1 and 2, which means that the dispersion presented in Table 8 should be higher. Additionally, when comparing the intensity ratio between the peaks for linearly bonded and bridge-bonded CO, there seem to be a bigger part bridge-bonded CO for Rh3 compared to Rh1 and Rh2.

It was earlier discussed that the dispersion over 100 % could be due to new active sites formed at the Rh-CeO_2 interface. A peak for bridge-bonded CO in the Rh-CeO_2 interface would appear around 1720 cm^{-1}. However, no such peak can be seen in around this wavenumber, see Figure 10, thus ruling out this theory.

Figure 11 below shows the DRIFTS spectrum of Rh2, pre-treated with O_2 and H_2 followed by CO_2 at low temperature, during and after both the CO_2 flow and the CO flow. Due to lack of time and technical difficulties, this sample is the only one measured with this pre-treatment but could give an indication of the behavior the other samples would have had. This is also the reason for no spectrum of the similar pre-treatment with CO_2 flow at high temperature.

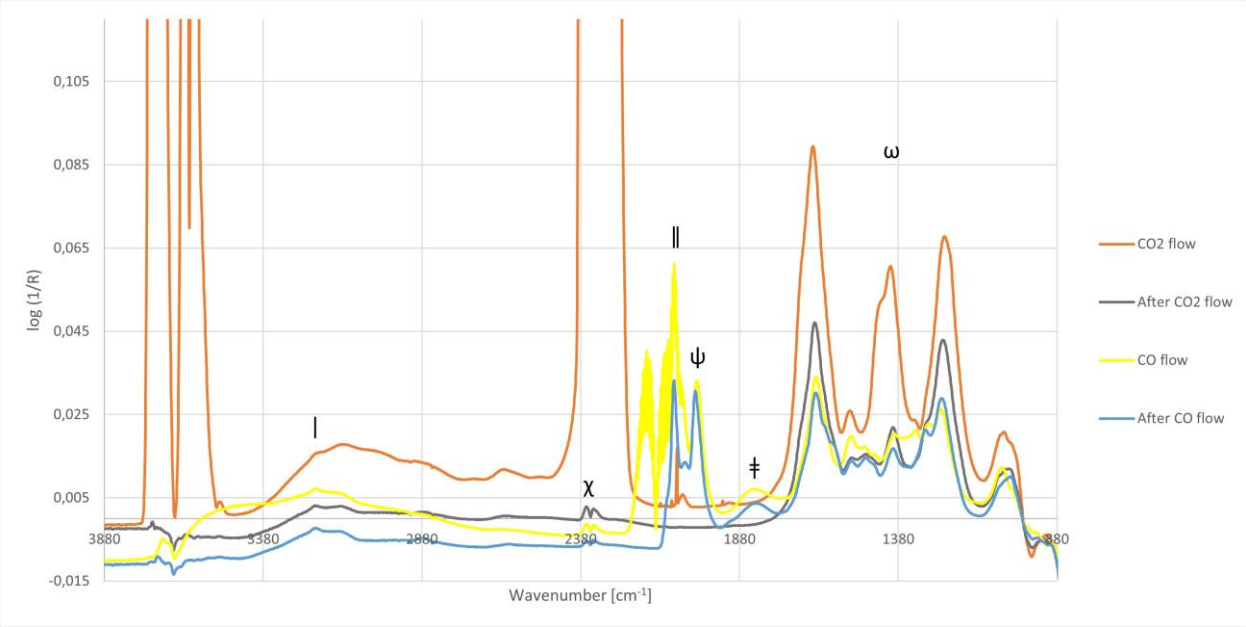

Figure 11: DRIFTS spectrum for Rh2, pre-treated with O_2, H_2 and CO_2.

The same kind of peaks shown in Figure 9 & 10 are also present here, along with one double peak at a wavenumber around 2349 cm^{-1}, as well as two double peaks around the wavenumber interval 3550-3750 cm^{-1} which are characteristic for CO_2. The CO_2 peaks are more clearly visualized in Figure A.1, see Appendix.

No CO peaks can be seen after the CO_2 flow, grey line. Note that not all CO_2 was removed since small CO_2 peaks still are present. It was earlier discussed that CO_2 could dissociatively adsorb onto the metallic Rh, thus oxidizing it as well as forming CO that could adsorb onto the metallic Rh before the actual CO chemisorption measurement. The absence of CO peaks indicates that no, or a negligible amount, CO adsorbs on the surface, which in turn could mean that the dissociation of CO_2 is insignificant. This thus rules out that theory. However, a complementary study such as ambient-pressure X-ray photoelectron spectroscopy (AP-XPS) could have been of interest since it is able to distinguish between different oxidation states. [29]

However, worth noticing is that the difference between the linearly adsorbed CO and the formed carbonates in Figure 11, blue line, is much smaller in comparison to Figure 10. This could be due to that the CO_2 has oxidized the metallic Rh, thus made it possible for more carbonates to form from the CO flow in relation to how many CO that are able to adsorb onto the metallic Rh.

Figure 12 below shows the DRIFTS spectrum of Rh2, pretreated with O_2, CO_2 and H_2. Just as for the other pre-treatments with CO_2, lack of time and technical difficulties made measurement of only one sample possible.

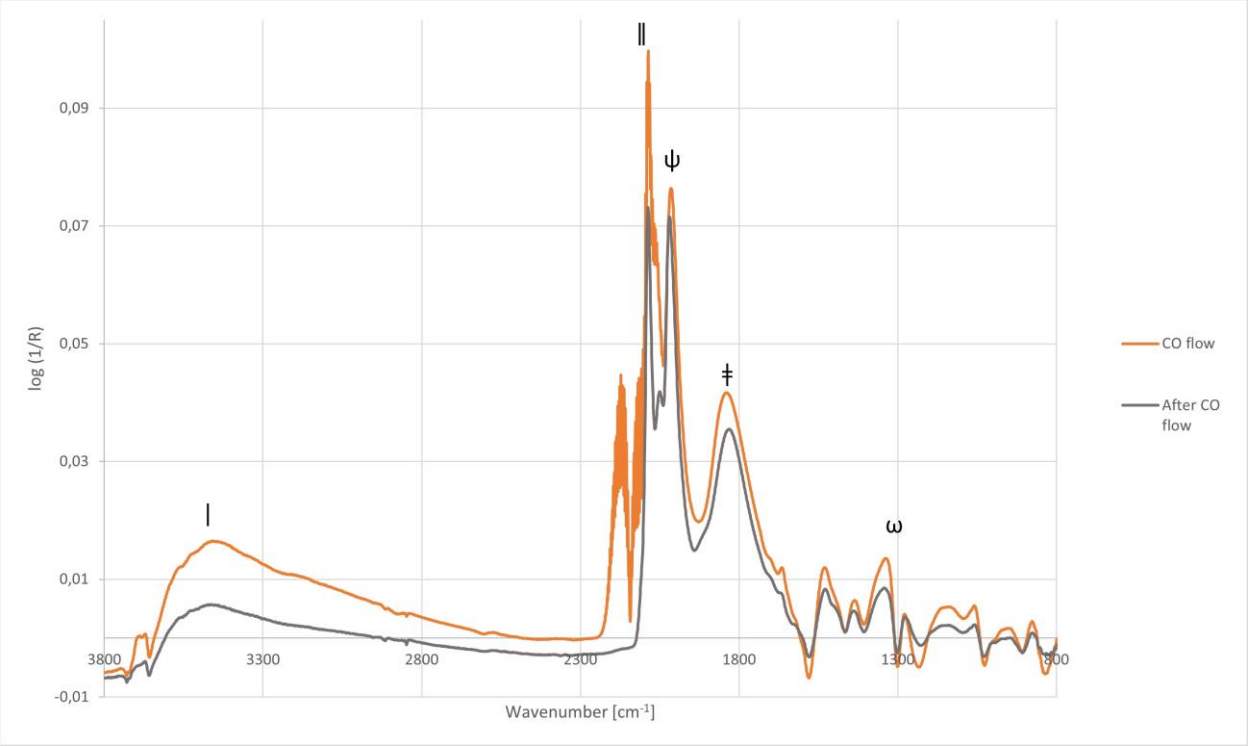

Figure 12: DRIFTS spectrum for Rh2, pre-treated with O_2, CO_2 and H_2.

When comparing the DRIFTS spectrum in Figure 12 with previous spectra, the difference between linearly bonded CO and carbonates formed during the CO flow seems to be higher than for the O_2, H_2, CO_2 pre-treatment, blue line in Figure 11, but slightly lower than for the O_2, H_2 pre-treatment. It then stands to reason that the H_2 flow manages to remove most, but not all, carbonates formed during the CO_2 flow. The CO chemisorption results presented in Table 8 confirm this theory.

4.5 Reactor measurements

4.5.1 Reaction rates

The obtained mass spectrum for Rh1 during the Sabatier reaction is showed below. Each group, containing three short H_2 pulses and one longer, represents the temperatures 150, 250, 350 and 400 °C from left to right.

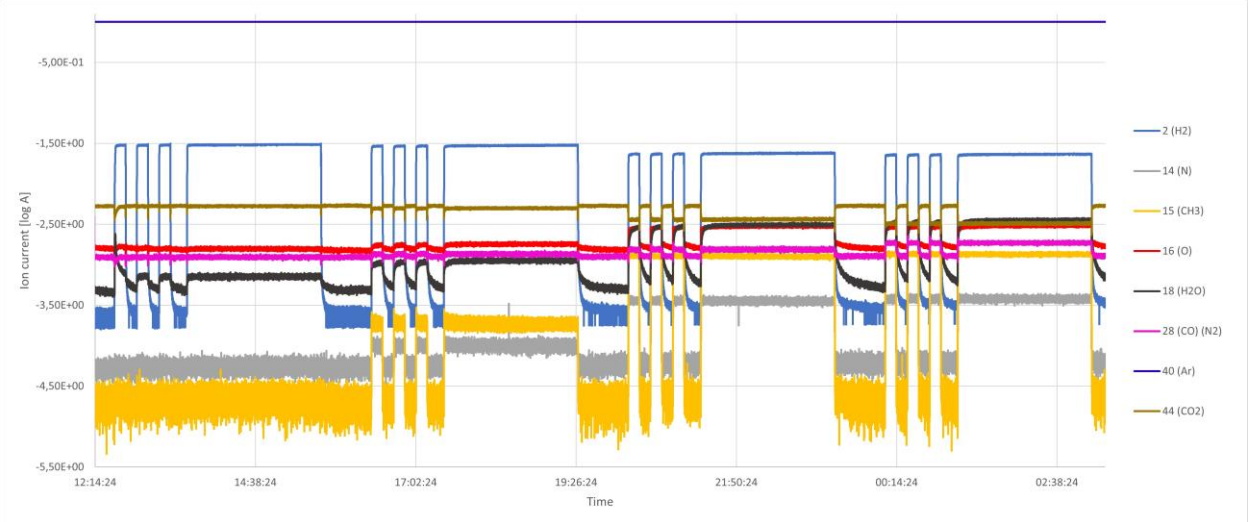

Figure 13: Mass spectrum of Rh1 during the Sabatier reaction.

It can be seen that the consumption of CO_2 starts to increase around 250 °C, thus indicating that the reaction is happening. The increasing temperature results in an increase in formation of CH_4, represented by the yellow line with mass 15 which indicates CH_3 that has formed through fraction of produced CH_4. The red line shows the mass 16 which is the same for both CH_4 and O. However, this line mainly represents the O released from the CO_2 through fractioning by the spectrometer's ionizer. The amount of produced water increases also with increasing temperature, which is due to the RWGPR being more favorable at high temperatures, as discussed in Section 2.1.2.

The amount of formed CO also increases with increasing temperature. This is not surprising since CO is the other product of the RWGPR. However, it doesn't seem to occur in the same amounts as water, which is because water also is one of the products of the CO_2 methanation.

The other samples, including $Rh/Ce_{1-x}Sm_xO_{2-\delta}$, $Rh/Ce_{1-x}Fe_xO_{2-\delta}$ and $Ce_{1-x}Rh_xO_{2-\delta}$ show the same overall trends as Rh1. Their mass spectra are presented in the Appendix, but shows a more detailed image of the trends during the H_2 pulses and steady state at 350 °C.

Figure 9 and 10 in the Appendix shows an example of how fluctuations in the data could be avoided by normalization with the Ar flow.

The calculated reaction rates for all samples as a function of temperature are presented in Figure 14.

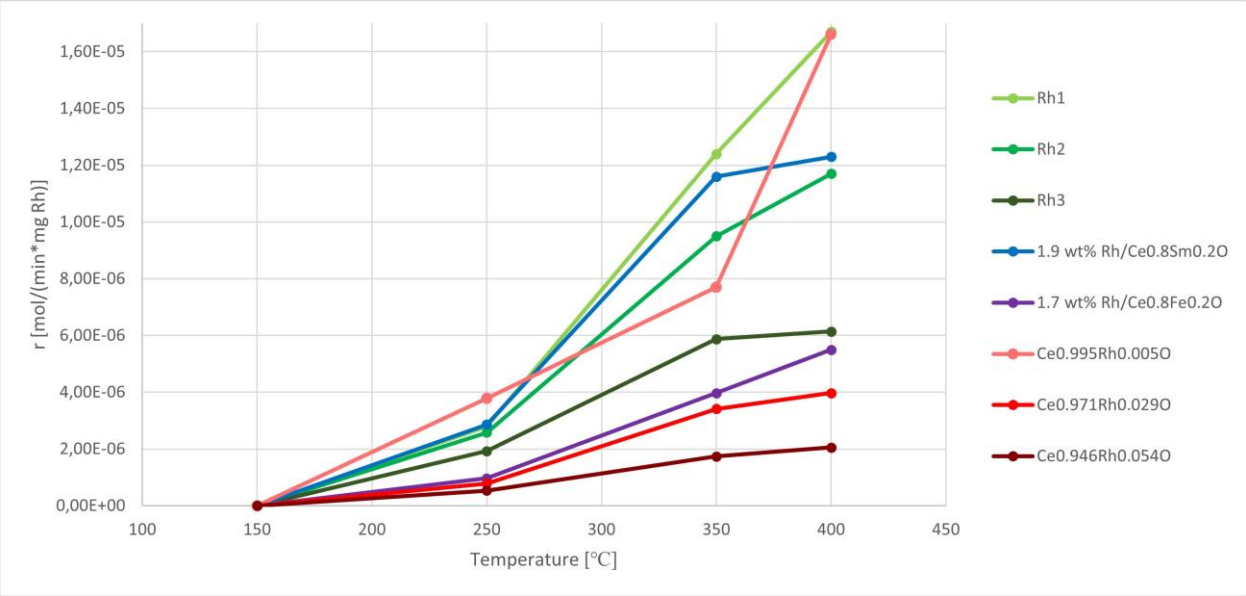

Figure 14: Reaction rate per g Rh vs. reactor temperature for all samples.

Since the CO_2 consumption, in general, was too low to be detected above the fluctuations in the 150 °C region, and that the temperature should be too low for any CO_2 methanation to occur, the calculated reaction rates were set to 0.

Overall, the reaction rate clearly increases with increasing temperature regardless of used catalyst. When comparing the Rh/CeO_2 samples with the $Ce_{1-x}Rh_xO_{2-\delta}$ samples, it can be seen that the reaction rate is generally lower when the Rh is a dopant in the

CeO_2. However, the $Ce_{0,995}Rh_{0,005}O_{2-\delta}$ shows a drastic increase in reaction rate at 400 °C.

When comparing the 1.7 wt% Rh/$Ce_{0.8}Fe_{0.2}O_{2-\delta}$ with Rh2, it can be seen that the Fe dopant reduces the reaction rate drastically. No CO chemisorption measurements were done on these samples and thus it is assumed that the Rh particle size is similar for the two samples since they have similar weight percentages and were impregnated through the same method. This assumption is also made for the 1.9 wt% Rh/$Ce_{0.8}Sm_{0.2}O_{2-\delta}$, which turns out to have a much higher reaction rate than 1.7 wt% Rh/$Ce_{0.8}Fe_{0.2}O_{2-\delta}$ and Rh2. Worth noting is that Rh1 and 1.9 wt% Rh/$Ce_{0.8}Sm_{0.2}O_{2-\delta}$ have a similar reaction rate at 250 °C and 350 °C but that it is much higher for Rh1 at 400 °C.

A comparison between the Rh/CeO_2 and $Ce_{1-x}Rh_xO_{2-\delta}$ samples shows that the reaction rate per g Rh decreases with increasing amount of Rh, regardless the Rh being impregnated onto the sample or incorporated into the CeO_2. This could indicate that the reaction rate is not dependent on the amount of Rh that is being added to the catalyst, but rather the size of the Rh particles.

Figure 15 below shows a comparison of reaction rate per m^2 Rh at each temperature for all Rh/CeO_2 samples.

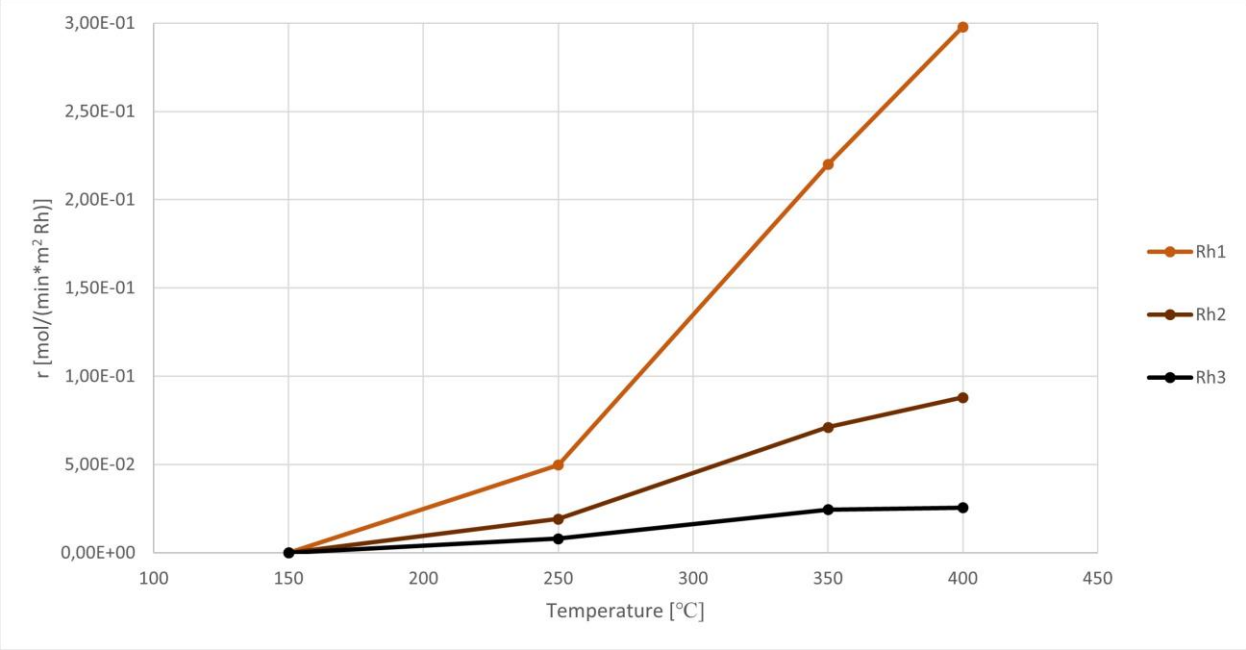

Figure 15: Reaction rate per m^2 Rh vs. reactor temperature for all Rh/CeO_2 samples.

The reaction rate per m^2 Rh decreases with increasing load of Rh, and thus with increasing Rh particle size as shown in Table 8. This means that Rh1 has the highest reaction rate, both per g Rh and per m^2 Rh, even though it has the lowest Rh load. The reaction rate is thus more dependent on the size of the Rh particles than the amount of Rh on the catalyst.

4.5.2 Selectivity

The calculated selectivities for all samples are presented in Figure 16.

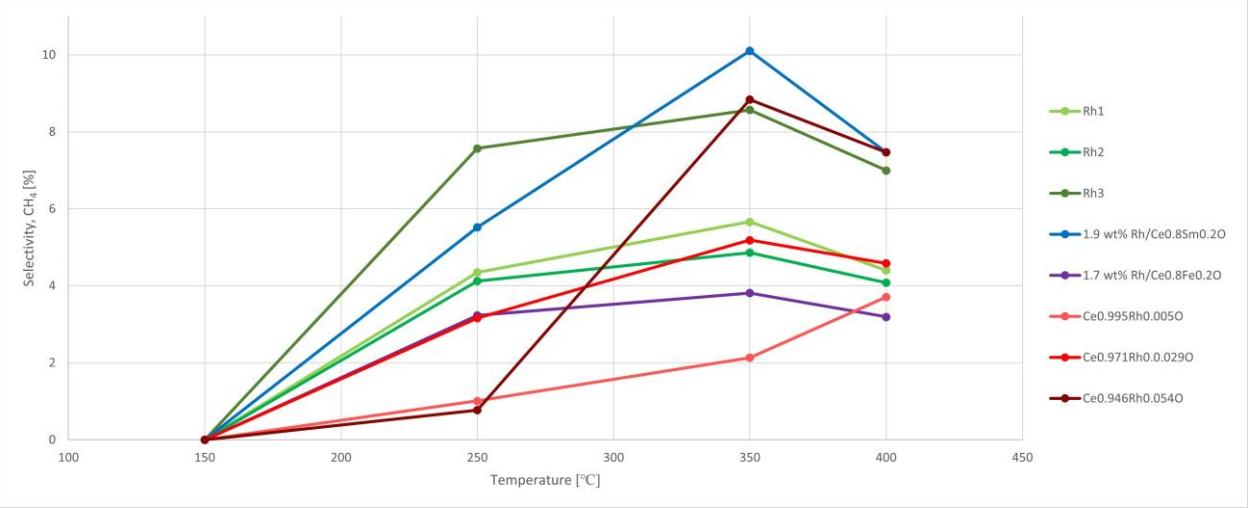

Figure 16: CH_4 selectivity vs. reactor temperature for all samples.

A selectivity maximum can be seen for all samples at 350 °C, with $Ce_{0.995}Rh_{0.005}O$ as the only exception. The presence of a maximum around this temperature is not unexpected since the RWGSR is more favorable at higher temperatures.

When comparing the Rh/CeO_2 samples with the $Ce_{1-x}Rh_xO_{2-\delta}$ samples, it can be seen that the selectivity is generally higher when the Rh is a dopant in the CeO_2. However, the $Ce_{0,995}Rh_{0,005}O_{2-\delta}$ shows a much lower selectivity than the others, as well as shows a different trend. More measurements would therefore have been desirable to verify this difference. Additionally, for all the Rh/CeO_2 and $Ce_{1-x}Rh_xO_{2-\delta}$ samples, the selectivity increases with increasing load of Rh, with Rh2 as the only exception.

A comparison between the 1.9 wt% $Rh/Ce_{0.8}Sm_{0.2}O_{2-\delta}$, 1.7 wt% $Rh/Ce_{0.8}Fe_{0.2}O_{2-\delta}$ and Rh2 shows that the use of a Sm dopant results in a considerably higher selectivity, just like for the reaction rates mentioned in previous section. Even here, the use of a Fe dopant impairs the catalytic properties.

Worth noting is that the selectivity is relatively low for all samples.

4.5.3 DRIFTS – Reactor measurements

The DRIFTS spectra for Rh1-Rh3 under reaction conditions are shown in Figure 17.

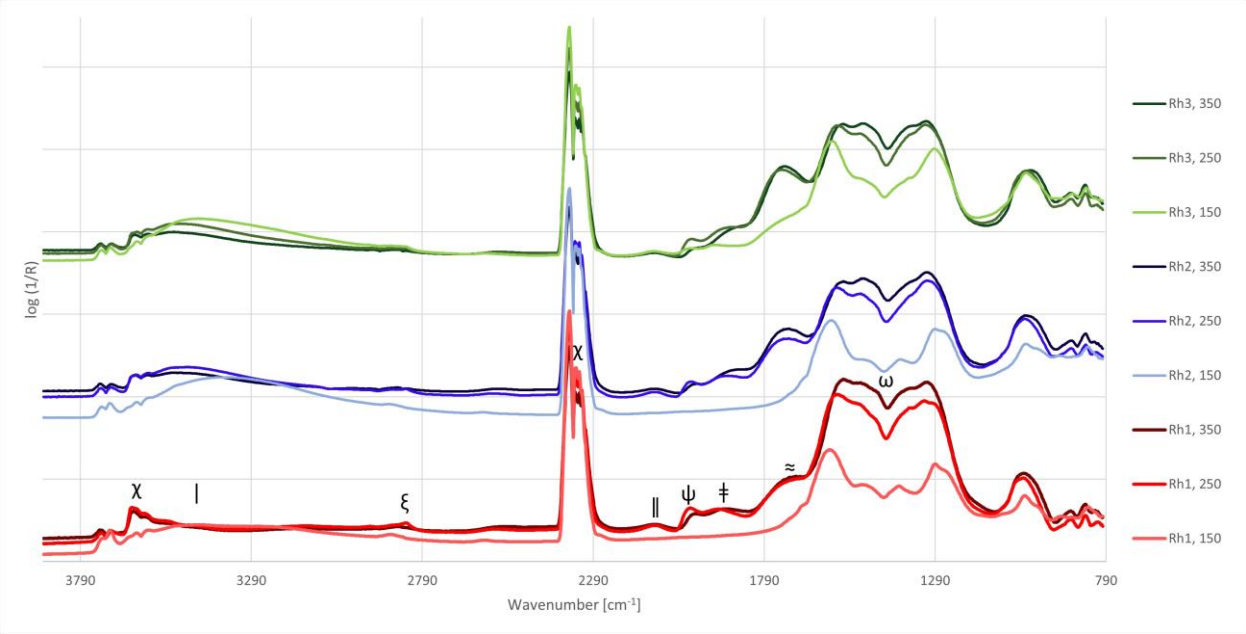

Figure 17: DRIFTS spectra for sample Rh1-Rh3 under reaction conditions at 150, 250 and 350 °C.

Table 10 shows the observed peaks and wavenumbers along with the corresponding species for each.

Table 10: IR absorption bands discussed in this study.

Peak	**Wavenumber [cm^{-1}]**	**Species**	**Ref.**
I	3000-3700	Hydroxyl region	[22]
II	2100-2200	Gaseous CO, with its corresponding peak on the left	[23]
ξ	2840-3000	C-H stretching, alkanes	[22]
χ	2349	Gaseous CO_2, with its two corresponding double peaks around 3550-3750 cm^{-1}	[22, 24, 25]
ψ	2020	Linearly bonded CO on Rh, with its corresponding peak on the left	[24, 26, 27]
ǂ	1750-1900	Bridge-bonded CO on Rh	[24, 26-28]
≈	1720-1740	C=O stretching, aldehydes	[22]
*	1720	Bridge-bonded CO on Rh-CeO_2 interface	[6]
ω	1200-1600	Carbonate-like species	[24, 26, 27]

Several peaks are known from the discussion regarding the CO chemisorption in Section 4.4.1. However, there are two new peaks worth attention. The first one is in the approximate interval of 2840-3000 cm^{-1}, which corresponds to the desired alkane. The second peak, observed in the approximate interval of 1720-1740 cm^{-1}, could correspond to aldehydes (RCHO), which could be a formate ($COOH^-$) precursor.

It was earlier shown that Rh3 had a higher selectivity maximum at 350 °C than Rh1 and Rh2. The spectra in Figure 17 show a slightly higher formate peak for Rh3 in relation to the peaks corresponding to linearly bonded and bridge-bonded CO on Rh. This could indicate a reaction pathway through the formate. However, more studies must be made

to confirm this theory. The exact methanation reaction pathway is still under discussion in several studies where two alternatives are: through the formation of formate intermediates, and through dissociated CO2 that forms CO, which is hydrogenated to methane. The pathway may also change depending on the used catalyst. [30-33]

5 Conclusions

This study has shown that the reaction rate for Rh/CeO_2 is affected by the size of the Rh particles, rather than the amount of Rh, and that a smaller size results in a higher reaction rate. On the contrary, the CH_4 selectivity increased with a higher amount of Rh.

The inclusion of Rh into the CeO_2 generally resulted in a lower reaction rate compared to Rh/CeO_2, but a higher selectivity. These two qualities must then be weighed against each other to determine the most optimal way of using the Rh for this reaction.

It has also been shown that the use of a Sm dopant in the CeO_2 improves the reaction rate while a Fe dopant decreases it. The same trend was shown for the selectivity, thus making $Rh/Ce_{1-x}Sm_xO_{2-\delta}$ the most suited catalyst for the methanation of CO_2.

However, further studies are necessary in order to make these results statistically significant.

6 References

1. Nations, U. *Global Warming Potentials (IPCC Second Assessment Report)*. Available from: https://unfccc.int/process/transparency-and-reporting/greenhouse-gas-data/greenhouse-gas-data-unfccc/global-warming-potentials.
2. Sonebi, M., Y. Ammar, and P. Diederich, *Sustainability of cement, concrete and cement replacement materials in construction*, in *Sustainability of Construction Materials*, J.M. Khatib, Editor. 2016, Woodhead Publishing: Woodhead Publishing Series in Civil and Structural Engineering. p. 371-396.
3. Stangeland, K., et al., *CO2 Methanation: The Effect of Catalysts and Reaction Conditions.* Energy Procedia, 2017. **105**: p. 2022-2027.
4. Younas, M., et al., *Recent Advancements, Fundamental Challenges, and Opportunities in Catalytic Methanation of CO2.* Energy & Fuels, 2016. **30**: p. 8815–8831.
5. Ghaib, K., K. Nitz, and F.-Z. Ben-Fares, *Chemical Methanation of CO2: A Review.* ChemBioEng Reviews, 2016. **3**(6): p. 266-275.
6. Martin, N.M., et al., *Catalytic hydrogenation of CO2 to methane over supported Pd, Rh and Ni catalysts.* Catalysis Science & Technology, 2017(5): p. 1086-1094.
7. Ashok, J., et al., *A review of recent catalyst advances in CO2 methanation processes.* Catalysis Today, 2020. **356**: p. 471-489.
8. Ross, J.R.H., *Heterogeneous Catalysis - Chemistry in Two Dimension*, in *Heterogeneous Catalysis - Fundamentals and Applications*, J.R.H. Ross, Editor. 2012: Elsevier. p. 1-15.
9. Ross, J.R.H., *Catalyst Preparation*, in *Heterogeneous Catalysis - Fundamentals and Applications*, J.R.H. Ross, Editor. 2012, Elsevier: ScienceDirect. p. 65-96.
10. Ross, J.R.H., *How does a catalyst work?*, in *Heterogeneous Catalysis - Fundamentals and Applications*, J.R.H. Ross, Editor. 2012: Elsevier. p. 47-64.
11. Andersson, D.A., et al., *Optimization of ionic conductivity in doped ceria.* 2006.
12. Sietsma, J.R.A., et al., *Application of ordered mesoporous materials as model supports to study catalyst preparation by impregnation and drying*, in *Scientific Bases for the Preparation of Heterogeneous Catalysts*, E.M. Gaigneaux, et al., Editors. 2006, Elsevier: ScienceDirect. p. 95-102.
13. Marceau, E., X. Carrier, and M. Che, *Impregnation and Drying*, in *Synthesis of Solid Catalysts*, P.D.K.P.d. Jong, Editor. 2009: Wiley Online Library.
14. Castro, M.D.L.d. and J.L.L. García, *Analytical freeze-drying*, in *Acceleration and Automation of Solid Sample Treatment*. 2002, Elsevier: ScienceDirect. p. 11-41.
15. Ross, J.R.H., *Surfaces and Adsorption*, in *Heterogeneous Catalysis - Fundamentals and Applications*. 2012, Elsevier: ScienceDirect. p. 17-45.
16. Sparks, D.L., et al., *Methods of Soil Analysis, Part 3: Chemical Methods*. 2020, John Wiley & Sons: Google. p. 1424.
17. Kwon, S., et al., *CO2 Sorption*, in *Coal Gasification and Its Applications*. 2011, Elsevier: ScienceDirect. p. 293-339.
18. Corporation, M.I., *Chemisorption*. Micromeritics.
19. Corp., P.A.W.-M.I., *Introduction to Chemical Adsorption Analytical Techniques and their Applications to Catalysis.* 2003: p. 12.
20. Accardo, G., et al., *Diffuse Reflectance Infrared Fourier Transform Spectroscopy for the Determination of Asbestos Species in Bulk Building Materials.* 2014.
21. Lercher, J.A. and A. Jentys, *Infrared and Raman Spectroscopy for Characterizing Zeolites*, in *Introduction to Zeolite Science and Practice*, J. Čejka, et al., Editors. 2007, Elsevier: ScienceDirect. p. 435-476.

22. Merck. *IR Spectrum Table & Chart*. 2022 [cited 2022; Available from: https://www.sigmaaldrich.com/SE/en/technical-documents/technical-article/analytical-chemistry/photometry-and-reflectometry/ir-spectrum-table.
23. Commerce, U.S.S.o., *Carbon Monoxide*. 2021: NIST-National Institute of Standards and Technology.
24. Martin, N.M., et al., *Catalytic hydrogenation of CO2 to methane over supported Pd, Rh and Ni catalysts.* Catalysis Science & Technology, 2017.
25. Commerce, U.S.S.o., *Carbon dioxide*. 2021: NIST-National Institute of Standards and Technology.
26. Martin, N.M., et al., *Structure–function relationship for CO2 methanation over ceria supported Rh and Ni catalysts under atmospheric pressure conditions.* Catalysis Science & Technology, 2019.
27. Basile, F., et al., *In Situ IR Characterization of CO Interacting with Rh Nanoparticles Obtained by Calcination and Reduction of Hydrotalcite-Type Precursors.* International Journal of Spectroscopy, 2011. **2011**.
28. Swart, I., et al., *The Effect of Charge on CO Binding in Rhodium Carbonyls: From Bridging to Terminal CO.* 2008.
29. Karslıoğlu, O. and H. Bluhm, *Ambient-Pressure X-ray Photoelectron Spectroscopy (APXPS)*, in *Operando Research in Heterogeneous Catalysis*. 2016, Springer, Cham: Springer Link. p. 31-57.
30. Pana, Q., et al., *Insight into the reaction route of CO2 methanation: Promotion effect of medium basic sites.* Catalysis Communications, 2014. **45**: p. 74-78.
31. Schmider, D., L. Maier, and O. Deutschmann, *Reaction Kinetics of CO and CO2 Methanation over Nickel.* 19 April 2021.
32. Yang, Y., et al., *Reaction mechanism of CO2 methanation over Rh/TiO2 catalyst.* Fuel, 2020. **276**.
33. Ren, J., et al., *Insights into the mechanisms of CO2 methanation on Ni(111) surfaces by density functional theory.* Applied Surface Science, 2015. **351**: p. 504-516.

7 Appendix

7.1 DRIFTS

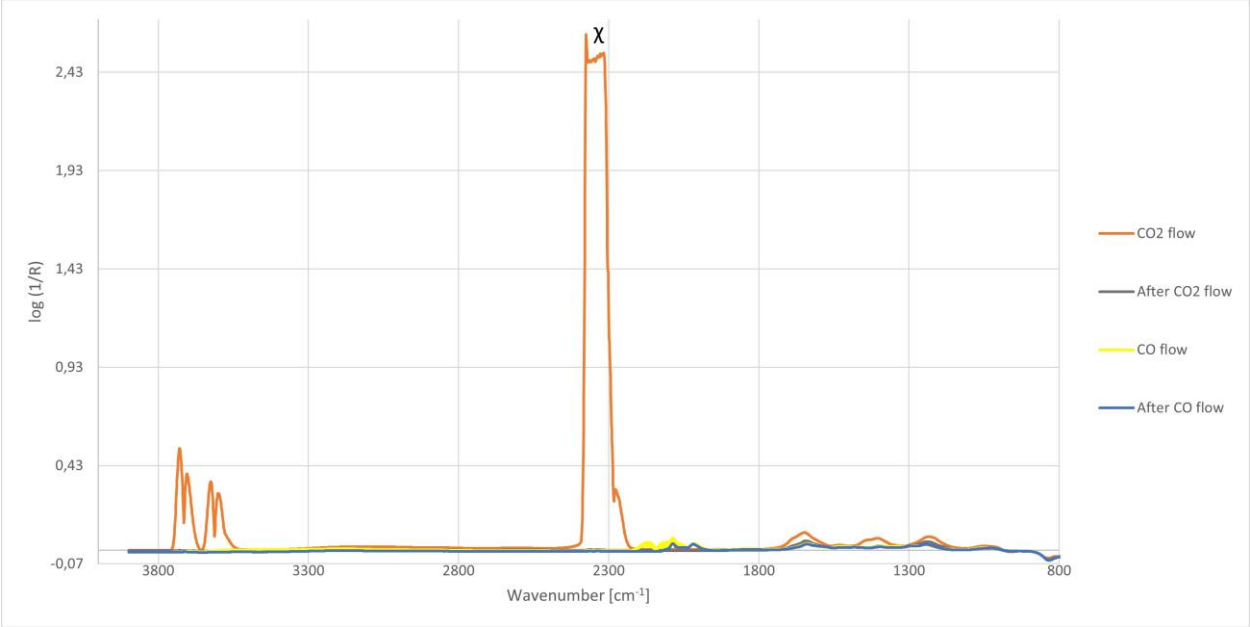

Figure A. 1: DRIFTS spectrum of Rh2 pretreated with O_2, H_2 and CO_2.

7.2 Reactor measurements

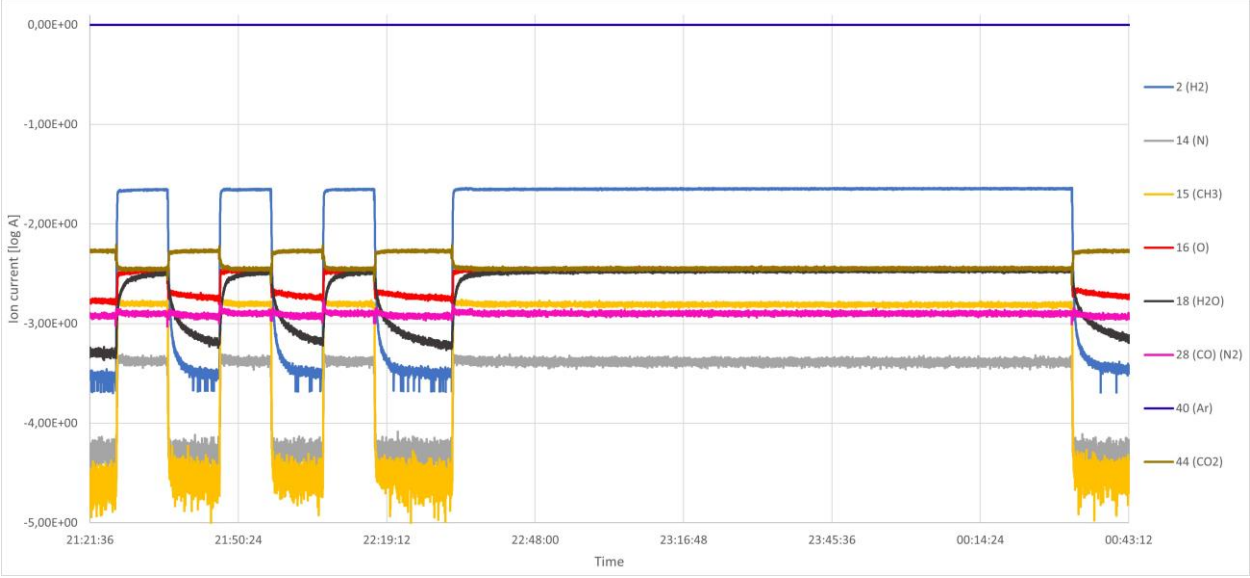

Figure A. 2: Mass spectrum of Rh2 during the Sabatier reaction at 350 °C.

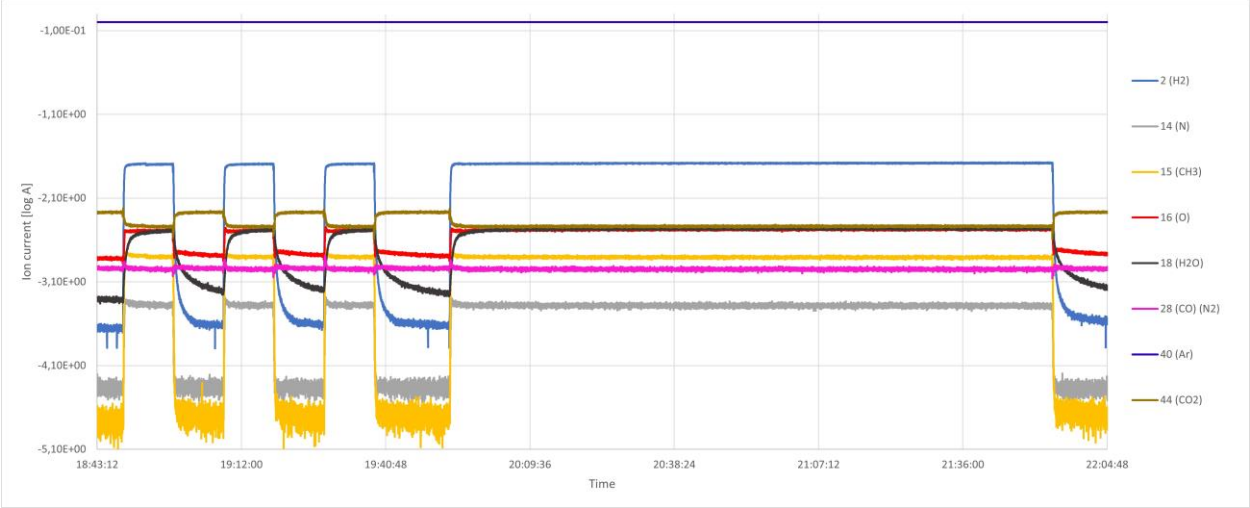

Figure A. 3: Mass spectrum of Rh3 during the Sabatier reaction at 350 °C.

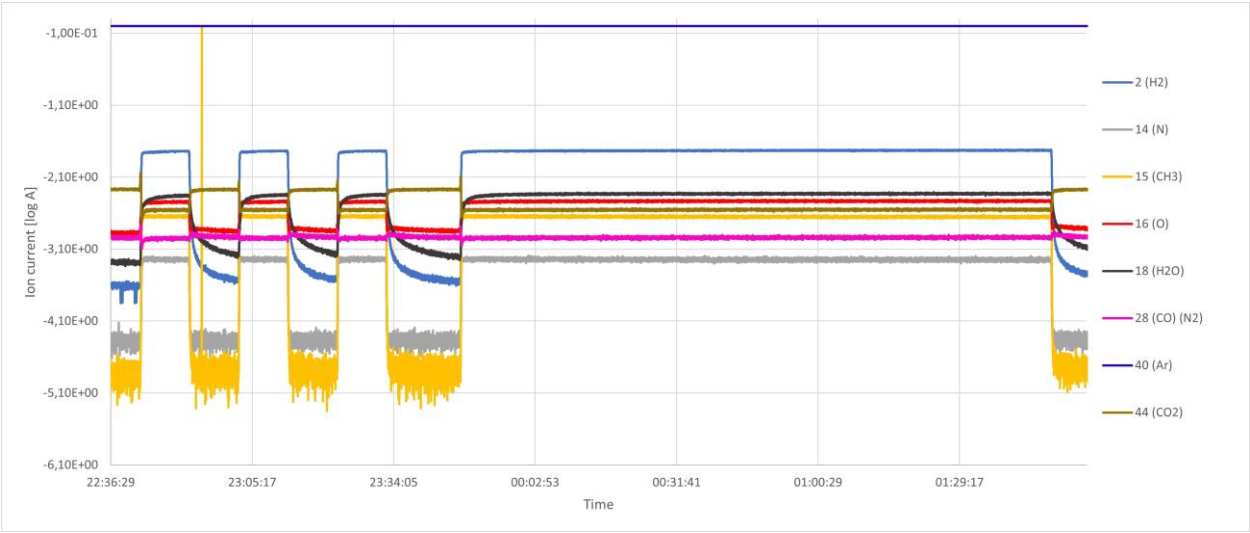

Figure A. 4: Mass spectrum of 1.9 wt% Rh/$Ce_{0.8}Sm_{0.2}O_{2-\delta}$ during the Sabatier reaction at 350 °C.

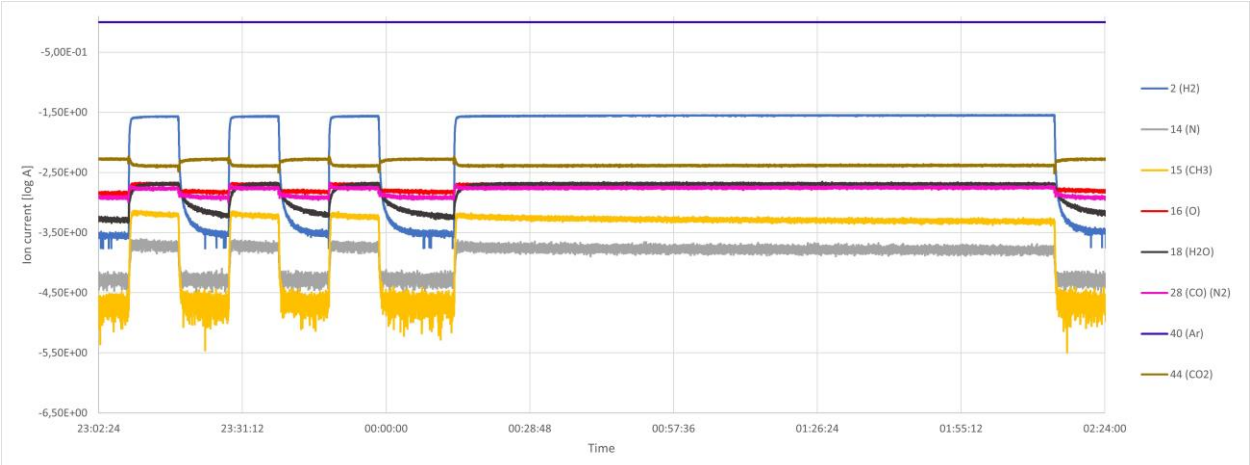

Figure A. 5: Mass spectrum of 1.7 wt% Rh/$Ce_{0.8}Fe_{0.2}O_{2-\delta}$ during the Sabatier reaction at 350 °C.

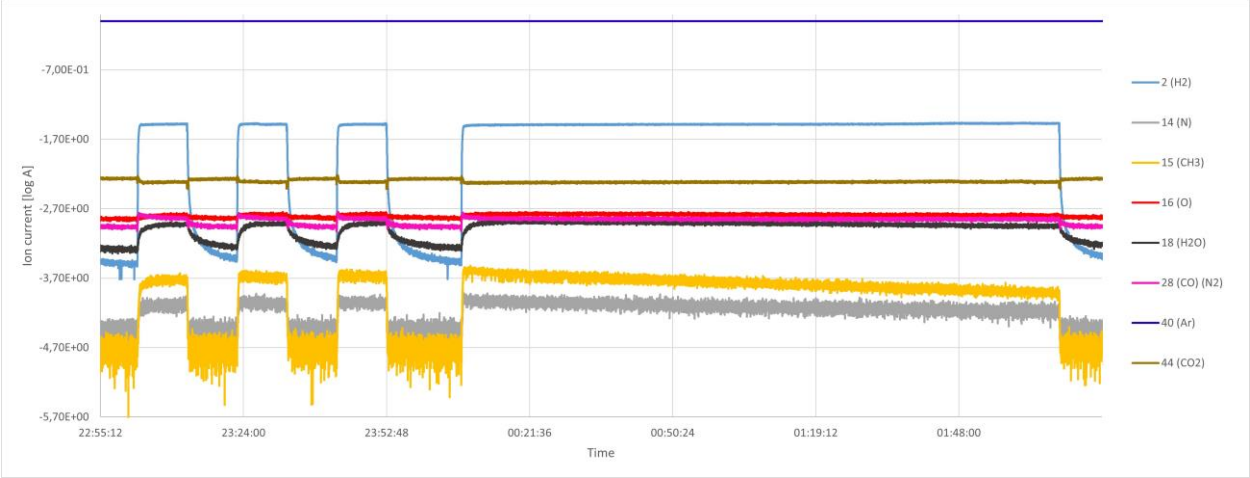

Figure A. 6: Mass spectrum of $Ce_{0.995}Rh_{0.005}O_{2-\delta}$ during the Sabatier reaction at 350 °C.

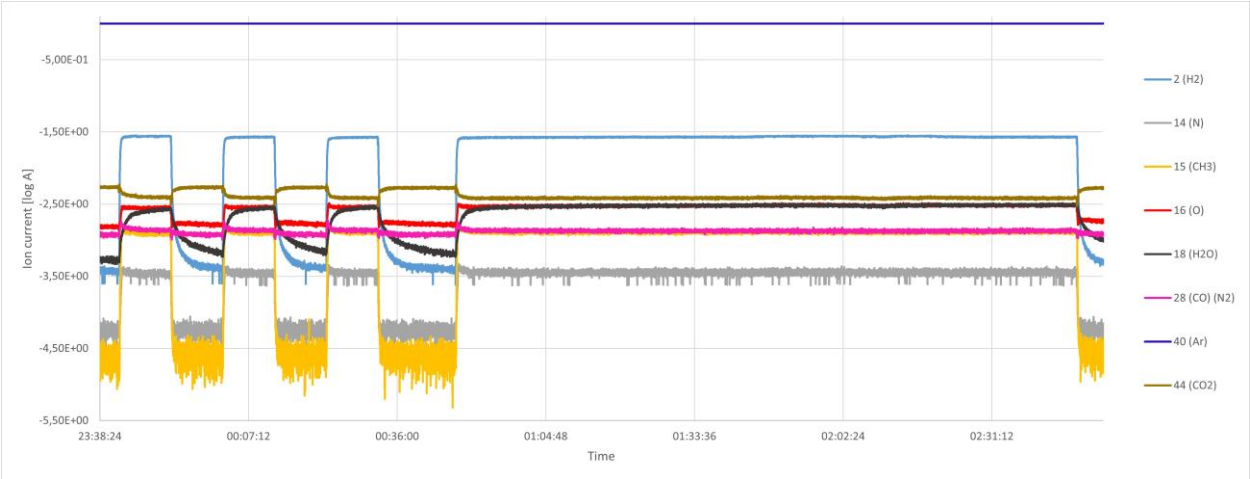

Figure A. 7: Mass spectrum of $Ce_{0.971}Rh_{0.029}O_{2-\delta}$ during the Sabatier reaction at 350 °C.

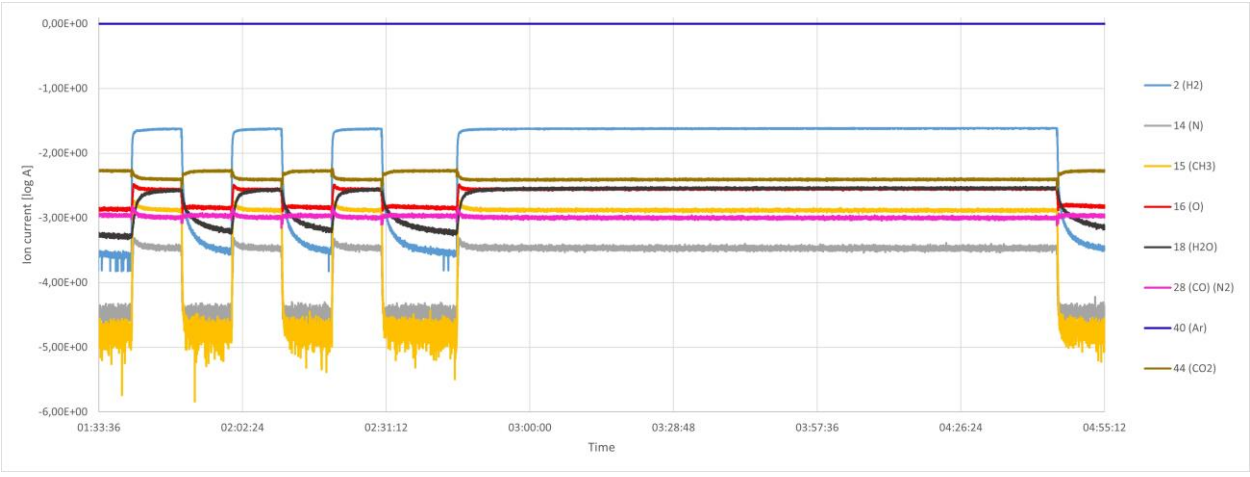

Figure A. 8: Mass spectrum of $Ce_{0.946}Rh_{0.054}O_{2-\delta}$ during the Sabatier reaction at 350 °C.

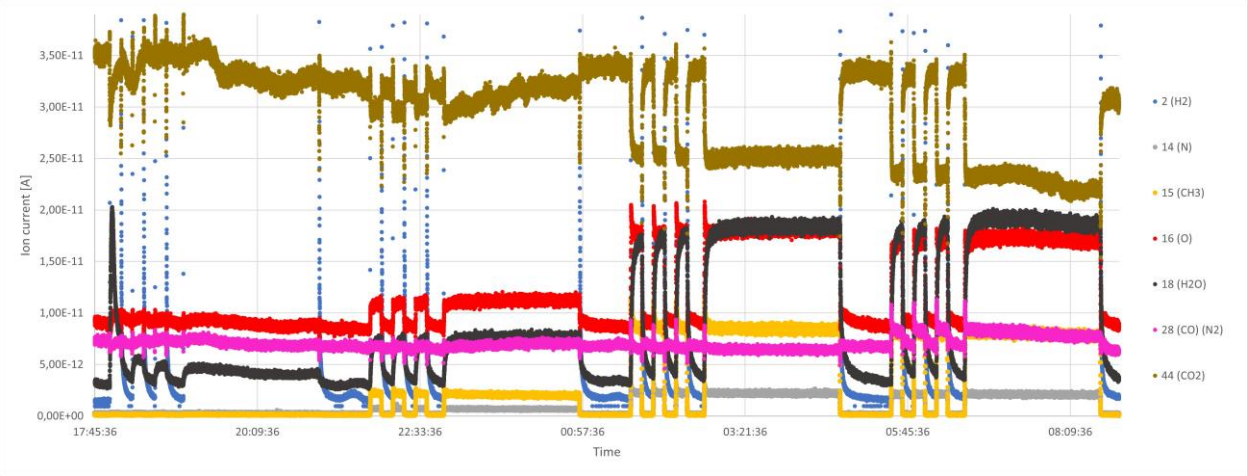

Figure A. 9: Mass spectrum of $Ce_{0.946}Rh_{0.054}O_{2-\delta}$ during the Sabatier reaction, without Ar normalization.

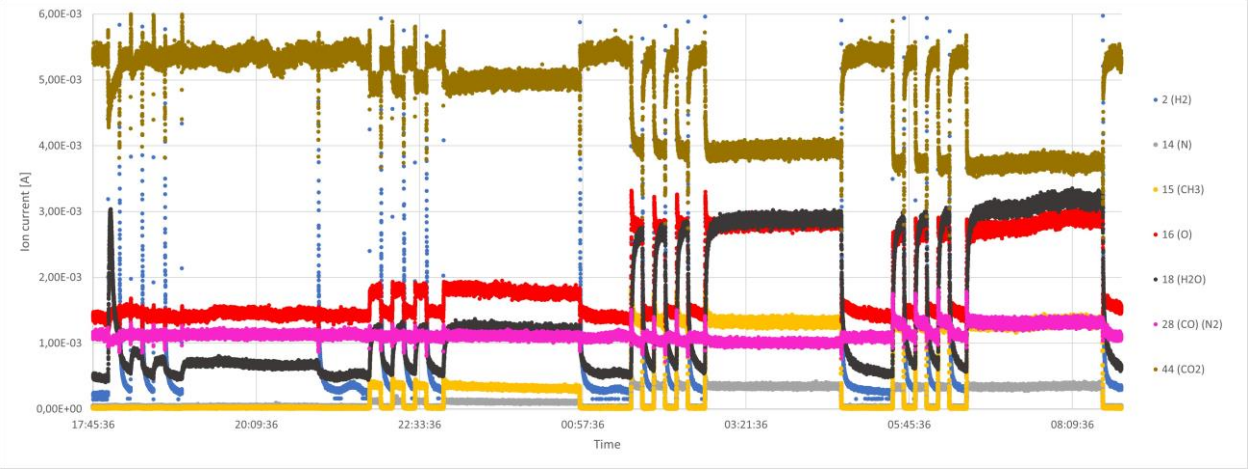

Figure A. 10: Mass spectrum of $Ce_{0.946}Rh_{0.054}O_{2-\delta}$ during the Sabatier reaction, with Ar normalization.

DEPARTMENT OF CHEMISTRY AND CHEMICAL ENGINEERING
CHALMERS UNIVERSITY OF TECHNOLOGY
Gothenburg, Sweden 2022
www.chalmers.se

CHALMERS
UNIVERSITY OF TECHNOLOGY